MECHANICAL PROPERTIES OF ROCKS RELATED TO DRILLING TECHNOLOGY

J. Handin and M. Friedman

Center for Tectonophysics
Texas A&M University
College Station, Texas
(713) 845-3251

Ninth Quarterly and Summary Progress Report

Period Covered: 30 June 1976 to 30 September 1976

October 15, 1976

Contract No. 82-9473

Work Sponsored by Sandia Laboratories

Requester: M. M. Newsom, Org. 5724

Contracting Representative: L. E. Barnes, Org. 3721

Prepared for

Sandia Laboratories
Albuquerque, New Mexico

REA

PREFACE

The objectives of this project, Mechanical Properties of Rocks related to Drilling Technology, are to investigate the mechanical properties of rocks under confining pressures to 5 kb, temperatures to 400°C and strain rates of 10^{-5} to 10^{2} sec^{-1}, and to learn exactly how the spark-drilling tool interacts with the rock to generate chips and "make hole." Both aspects are designed to help optimize spark drilling. Dr. J. Handin (8.4% time) is responsible for supervising the experimental rock deformation; Dr. M. Friedman (12.5% time) is studying spark-drilled holes, and he supervises the work on deformation mechanisms in experimentally deformed specimens. Mr. T. L. Blanton III (graduate research assistant) devotes half of his time to the project.

This project was initiated 1 July 1974, to provide a continuing record, the summary of progress for the both years is given below followed by a detailed report of the work completed during the second year (1 July 1975 to 31 August 1976). The latter consists of the results of the experimental deformation of rocks at confining pressure and at strain rates to 10^{2} sec^{-1}. It represents the Ph.D. Dissertation of Mr. Blanton.

During the forthcoming year (1 September 1976 to 30 September 1977) Dr. J. Handin will continue to be responsible for supervising the experimental rock deformation; Dr. M. Friedman (12.5 percent) will study the spark drilled holes and the deformation mechanisms in experimentally deformed specimens; and Mr. J. N. Magouirk, research technician, will be devoting half his time to the project.

SUMMARY

1. Rocks to be studied are identified, acquired, and petrographically described. They are the Charcoal Granodiorite (St. Cloud Grey Granodiorite), Indiana Limestone, Berea Sandstone, and a quartz diorite supplied by the Sandia Laboratories.

2. Three types of fractures result from the initial spark drilling* in all rocks. In order of their relative abundance these are: cone fractures (which geometrically lie on the surfaces of downward opening nested cones of 60 to 30° apical angle that are co-axial with the axis of drill-hole), spall fractures (which are oriented normal to the axis of the drill-hole), and high-angle fractures (which are inclined toward the downward end of the drill-hole-axis and at 45 to 90° to the bottom of the drill hole). Cone and spall fractures exhibit displacement only normal to the fracture surface as do most high-angle fractures, however, a very few of the latter do show shear offset and gouge development. The cone and spall fractures both are parallel to the greatest principal compressive stress trajectories for the ingoing and relaxation of the compressive pulse, respectively. Conclusion: the fractures produced by the spark drilling are mainly extension (tensile) fractures. (See details in Second, Third, and Fifth Quarterly Reports.)

3. The relative abundance and scale of development of these three

*Single-pair-electrode bits operated at 2 to 5 pulses/min with 150 joules energy at a distance of 0.6 to 10.0 cm from the rock; and four-pair-electrode bits operated at 600 pulses/min with 900 joules energy and resting on the rock.

types of fractures vary with rock type. Variations between those in the Charcoal Granodiorite and the Sandia Quartz Diorite are not understood because these rocks are different most conspicuously only in grain size. The conspicuous development of spall fractures in spark-drilled Berea Sandstone is explicable in that the spalls parallel the planar anisotropy of bedding in the sandstone.

4. In all rocks, chips are produced by the interaction of spalls, cones, and high-angle fractures.

5. Based on material in hand, it appears that spall fractures are developed only within 1 to 2 cm of the bottom of a drill hole and that cone and high-angle fractures propagate to greater depths (> 11.0 cm in the granodiorite). The abundance of all types of fracture decreases downward away from the bottom of the hole.

6. Study of thin sections cut across fractures in the spark-drilled rocks indicates that little if any "plastic" deformation accompanies the fracturing. This is particularly evident in the calcite of the Indiana Limestone which under slower strain rates, undergoes twin gliding (producing conspicuous twin lamellae) at differential stresses as low as 200 bars. Twin gliding does take place within 1 or 2 mm of the bottom of the drill hole when the low-powered single-electrode-pair-bit is used, but twin lamellae are absent when the higher powered four-electrode-pair-bit is used. The absence of twin gliding here may be due to the relatively slow kinetics of twinning compared to the velocity of the 3 to 5 kb-pressure pulse. In any event the absence of "plastic" mechanisms means that little spark energy is lost in a process that does not directly produce fracture, i.e., chip formation.

7. In brief, the principal mechanism of deformation induced by the spark energy is extension (possibly tensile) fracturing. This is most energy-efficient in that the tensile fracture strength of rock is lower than that for most other mechanisms of deformation.

8. The program of experimental deformation of Charcoal Granodiorite, Berea Sandstone and Indiana Limestone at confining pressures to 4.5 kb and strain rates from 10^{-1} to 10^{2} sec^{-1}, (room temperature, room dry-specimens) is completed. Data and conclusions are based on 32 experiments on the granodiorite, 35 tests on the sandstone, and 37 tests on the limestone. This work is reported in detail below. Major conclusions are:

9. The apparent sudden increase in failure stress above a strain rate of about 1 sec^{-1} reported in the literature and found in our tests is most likely due to machine inertia and does not reflect a real increase in material strength. That is, the room-temperature true-failure strengths of the three rocks tested are relatively insensitive to changes in strain-rate between 10^{-2} and 10 sec^{-1}.

10. The failure strains tend to decrease above a strain rate of about 1 sec^{-1} for the unconfined tests for all three rocks. At confining pressure the failure strains remain relatively constant between 10^{-2} and 10 sec^{-1}.

11. The two sedimentary rocks tend to be more brittle at the higher strain rates; the granodiorite exhibits the same degree of brittleness throughout.

12. The energy necessary to fragment these rocks is either constant or tends to decrease with increasing strain rate.

13. The above results are favorable to the spark-drilling technique in that not only is the extension-fracture mechanism of rock failure induced by the spark most efficient, but the failure strength of the rock at spark shock-rates (still about 10^3 to 10^4 faster than our fastest test) may not be as high as work prior to our study would have suggested.

ABSTRACT

Effect of Strain Rates from 10^{-2} to 10 s^{-1} in
Triaxial Compression Tests on Three Rocks. (December 1976)
Thomas Lindsay Blanton, III, B.S., Washington and Lee University;
M.S., Syracuse University
Chairman of Advisory Committee: Dr. John M. Logan

Room-temperature, compression tests at strain rates from 10^{-2} to 10 s^{-1} are run on Charcoal Granodiorite to 0.45 GPa confining pressure and on Berea Sandstone and Indiana Limestone to 0.25 GPa confining pressure. For each rock at each confining pressure, the differential stress at failure is relatively constant up to a strain rate of 1 s^{-1} and apparently increases abruptly above this strain rate. Dynamic analysis of the testing apparatus indicates that the apparent sudden increase in strength is due to machine inertia and does not reflect a real increase in the strength of the rocks. Similar increases, beginning between 10^{-1} and 10^{3} s^{-1}, are reported in previous studies. It is possible that these increases are also due to inertial effects.

Taking inertia into account, the actual failure stresses of the three rocks are relatively independent of strain rate between 10^{-2} and 10 s^{-1}. In the same interval, the strains at which the rocks begin to fragment tends to be lower at higher strain rates. The combination of decreasing strains and relatively constant stresses with increasing

strain rate suggests that the energy necessary to fragment the rocks is lower at higher strain rates.

ACKNOWLEDGMENTS

I wish to thank Dr. John M. Logan and other members of my committee, Dr. John W. Handin, Dr. C. Branning Johnson, Dr. Wayne M. Saslow, and Dr. Richard A. Schapery, for their helpful suggestions and thoughtful criticism of this dissertation.

Special thanks go to Dr. Schapery who originally suggested that I look at the problem of inertial effects.

Additional gratitude is due Dr. Melvin Friedman for his critical reading of the manuscript.

This work was supported financially by Sandia Corporation, contract no. 82-9473.

To Marianne

TABLE OF CONTENTS

LIST OF TABLES

LIST OF FIGURES

LIST OF FIGURES (continued)

INTRODUCTION

The purpose of this study is to investigate the mechanical behavior of three rocks deformed at strain rates intermediate to those achieved in conventional static and dynamic tests. This involves a relatively narrow range of strain rates from 10^{-1} to 10^{2} s^{-1}, but these strain rates are important because the strength of rock has been reported to increase rather abruptly with increasing strain rate across this interval. Inertial forces play an important role at these strain rates, and the findings of this study suggest that inertia in the testing apparatus can account for apparent increases in strength similar to those reported.

Interest in the behavior of rocks deformed at these strain rates stems mainly from engineering problems in rock excavation. Two concerns of the engineer are time involved and energy consumed in fragmenting the rock. Suppose, for example, that the technique is drilling. If the fracture stress of the rock increases at higher strain rates, the drilling techniques involving higher strain rates will consume more energy in removing a given amount of rock. The additional energy requirements at the higher rates may not be offset by the time saved. If, on the other hand, the rock becomes more brittle at higher strain rates, so that the strain before fragmentation of the rock is lower, then with higher strain-rate techniques the energy required to remove a given amount of rock may be lower. If so, these drilling

---

The citations on the following pages follow the style of the International Journal of Rock Mechanics and Mining Sciences.

techniques would be advantageous with respect to a savings of both energy and time.

The behavior of rocks at these strain rates is also important to geologists, who are beginning to consider a broader range of possible strain rates in natural rock deformation. A value of 3×10^{-14} s^{-1} has been referred to as a "representative geological strain rate" by Heard [7], but in a recent survey of rates of deformation, Price [16] gives estimates of 10^{-1} to 10^{3} s^{-1} for events such as brittle fracture, meteoric impact, and explosive volcanic eruptions. It should be pointed out that the strain rate of 3×10^{-14} s^{-1} is based on movements along the San Andreas Fault [21] and isostatic deformation of Lake Bonneville [4]. This figure may be appropriate as an average over long time, but many geologic structures may well result from the cumulation of numerous pulses of rapid deformation.

PREVIOUS WORK

The problem of achieving these intermediate strain rates is the laboratory is formidable, and as a result, information on the behavior of rocks in this range is sparse. Screw-driven and hydraulic devices used in conventional static tests commonly operate at strain rates less than 10^{-1} s^{-1}, whereas the impact techniques used in dynamic tests usually produce strain rates greater than 10^{2} s^{-1}. Table 1 summarizes papers which give rocks strengths for strain rates between 10^{-1} and 10^{2} s^{-1}. The usual method of predicting rock properties at intermediate strain rates is by interpolating between static and dynamic tests [5, 6, 8, 10, 11, 14, 19, 20]. On the low side of the intermediate range, the effect of changes in strain rate is not dramatic. The strength is either constant or slightly increasing with increasing strain rate. Tests on three rocks suggest that this trend continues at higher strain rates. Shockey et al. [19] report a constant tensile strength for the Arkansas Novaculite between strain rates of 10^{-4} and 10^{4} s^{-1}. The Dresser Basalt studied by Lindholm et al. [11] and a volcanic tuff tested by Green and Perkins [5] show a constant rate of increase in compressive strength with increasing log strain rate over a range of strain rates from 10^{-4} to 10^{3} s^{-1} (Fig. 1). If this were the case in general, there would be little reason for expending effort on tests at intermediate strain rates, but other studies [5, 8, 10, 14, 20] show a significant change in this trend at higher strain rates (Figs. 1 and 2). Somewhere between 10^{-1} and 10^{3} s^{-1}, depending on the study, the compressive strength begins

TABLE 1. TEST CONDITIONS IN EXPERIMENTAL STUDIES THAT PREDICT STRENGTH OF ROCKS AT INTERMEDIATE STRAIN RATES

Paper	Rock Type	Strain Rate (sec^{-1})	Confining Pressure (GPa)	Temperature (°C)	Type of Test	Type of Loading
Birkimer [1]	quartz monzonite	9.2 x 33.3	0	room	tension	gas gun
Green and Perkins [5]	Solenhofen Limestone	10^{-6} to 1.6 x 10^{-4}	0	room	compression	screw driven
	Westerly Granite,	1.8 x 10^{-2} to 3 x 10^{-1}	0	room	compression	gas ram
	and volcanic tuff	2 x 10^{2} to 10^{3}	0	room	compression	Hopkinson bar
Green et al. [6]	Solenhofen	10^{-4}	0 to 0.3	room	compression	gas ram
	Limestone	10^{-1}	0 to 0.3	room	compression	gas ram
	Westerly Granite	10^{-4}, 6 x 10^{-4}	0, 0.035, 0.2	room	compression	gas ram
		10^{-1}, 4 x 10^{-1}	0	room	compression	gas ram
		3	0.035	room	compression	gas ram
Kobayashi [8]	sandstone, marble,	10^{-4}	0	room	compression	hydraulic ram
	andesite, granite, tuff	10	0	room	compression	underwater explosive
Kumar [10]	basalt and	10^{-6}, 5 x 10^{-4}, 5	0	23, -196	compression	hydraulic ram
	granite	3 x 10^{2} to 2 x 10^{3}	0	23, -196	compression	Hopkinson bar
Lindholm et al. [11]	Dresser Basalt	1.9 x 10^{-4}	0 to 0.690	-190 to 1110	compression	hydraulic ram
		2.4 x 10^{-1}	0 to 0.345	-193 to 527	compression	hydraulic ram
		6.7 x 10^{2} to 10^{3}	0 and 0.138	-193 to 527	compression	hydraulic ram
Logan and Handin [12]	Solenhofen Limestone	10^{-2} to 1	0 to 0.3	room	compression	gas ram
	Westerly Granite	10^{-2} to 1	0 to 0.5	room	compression	gas ram
Perkins et al. [14]	porphyritic	10^{-4}, 3 x 10^{-4}	0	25, -78, -191	compression	gas ram
	tonalite	10^{-1}, 6 x 10^{-1}	0	25, -78, -191	compression	gas ram
		10^{3} to 1.6 x 10^{3}	0	25, -78, -191	compression	Hopkinson bar
Shockey et al. [19]	Arkansas	10^{-4}	0	room	tension	expanding ring test
	Novaculite	10^{4}	0	room	tension	gas gun
Stowe and Ainsworth [20]	granite, basalt,	2 x 10^{-7} to 5 x 10^{-4}	0 to 0.035	room	tension, compression	hydraulic ram
	and tuff	6.3 x 10^{-2} to 3.38	0	room	compression	drop tower, hydraulic ram
		~ 2 x 10^{4}	0	room	compression	gas gun

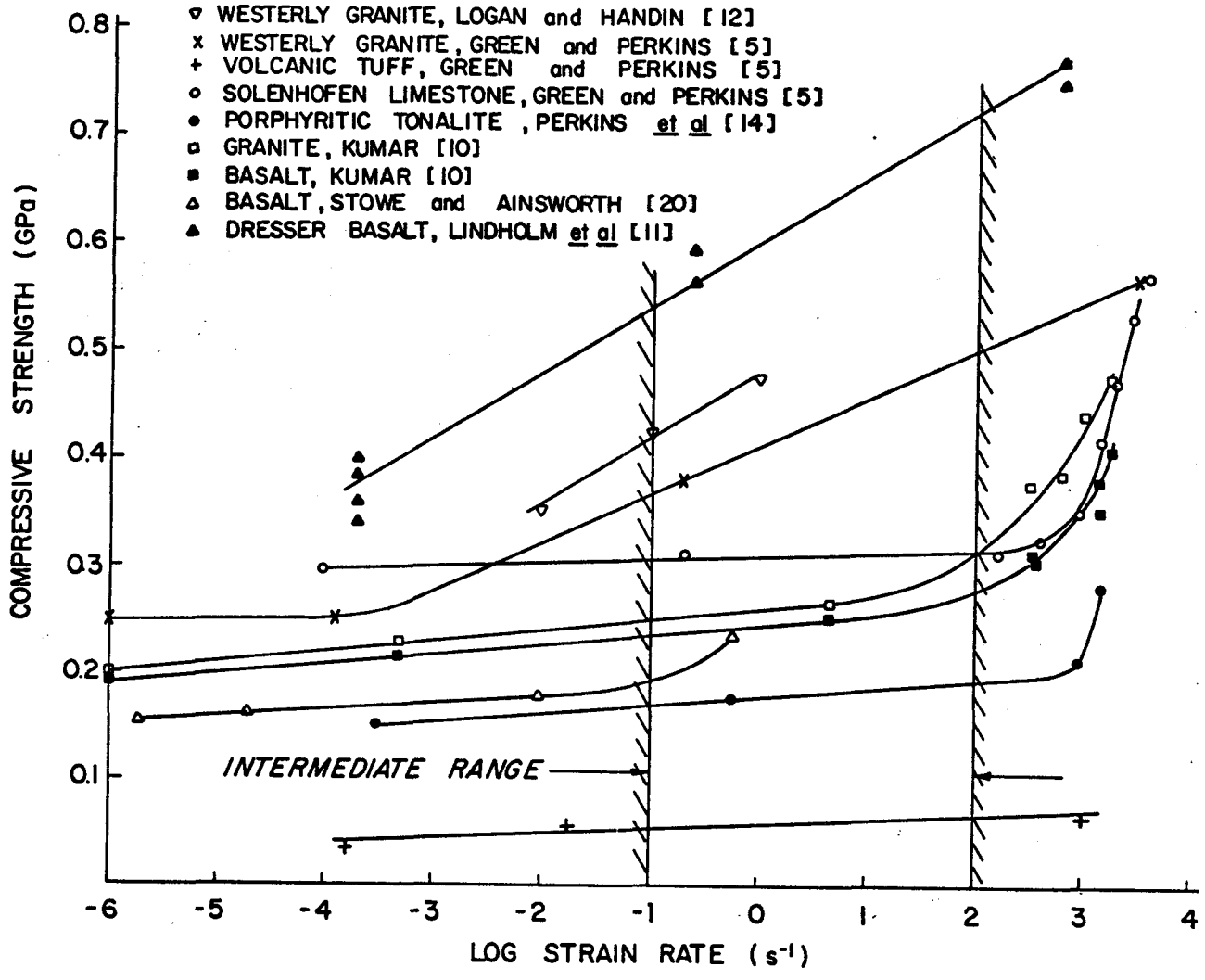

Figure 1. Uniaxial compression tests from earlier studies showing different strain-rate sensitivities of compressive strength.

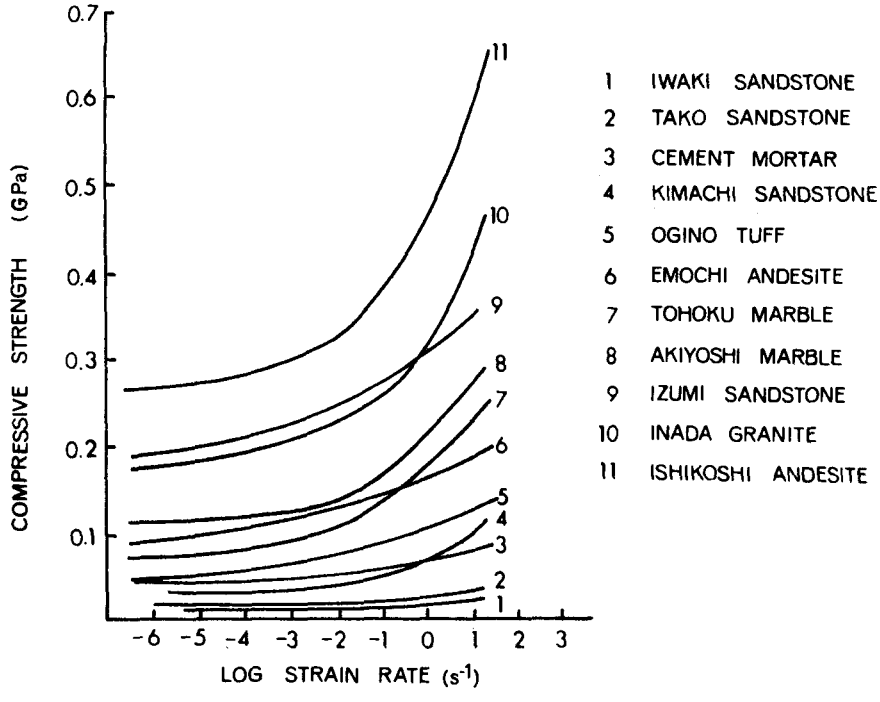

Figure 2. Experimental variation of compressive strength with strain rate from Kobayashi [8].

to increase more rapidly with increasing strain rate.

Three hypotheses have been proposed to account for this change in the strain-rate sensitivity of strength. (1) Kumar [10] maintains that in order for the strain rate to increase above a limit determined by the maximum crack-propagation velocity, the number of cracks must increase. This in turn requires an increase in stress. (2) Several workers [3, 5, 18] have explored the idea that the increase in strength is due to a transition from a state of uniaxial stress to a state of uniaxial strain at the higher strain rates. (3) Perkins et al. [14] suggest that a transition to a more strain-rate sensitive deformation mechanism is the reason for the more rapid increase in strength at higher strain rates, but they do not describe any particular mechanisms.

A fourth hypothesis, suggested by Schapery (personal communication), attributes the apparent increase in strength at higher strain rates to an axial inertial effect. This idea is supported by the results of this study and is developed more fully in a later section.

In anticipation of the results to follow, some previous work by Price and Knill [15] (Fig. 3) and Mellor and Hawkes [13] (Fig. 4) is presented here. Because these investigators have plotted loading and displacement rates respectively, their tests cannot be directly compared to others in terms of exact strain rates. Nevertheless, some relative comparisons can be made. There appears to be some tendency for increasing strength with increasing deformation rate, but what seems to be more characteristic of these tests are the

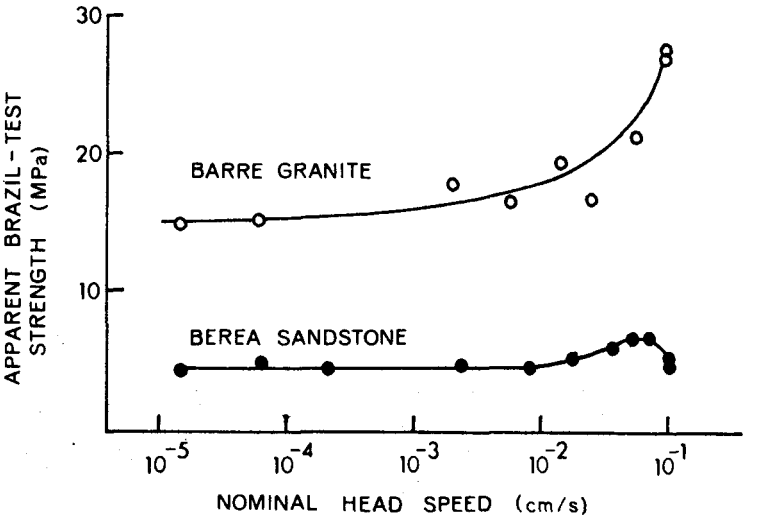

Figure 3. Experimental variation of apparent Brazil-test strength with displacement rate by Mellor and Hawkes [13].

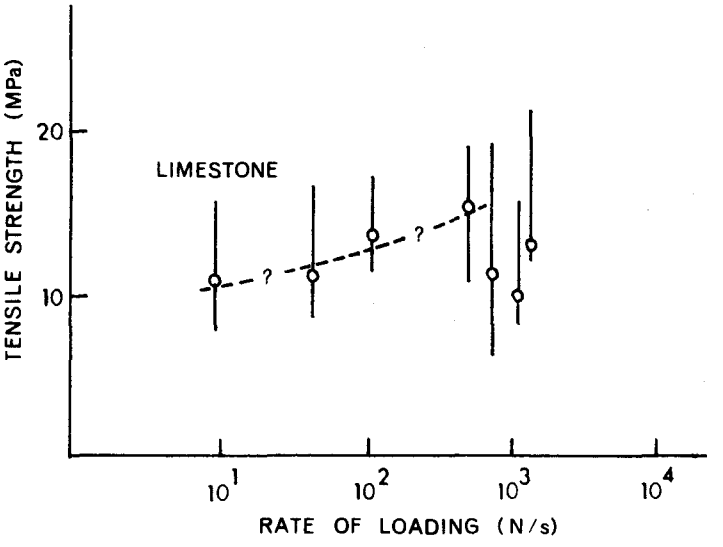

Figure 4. Experimental variation of tensile strength with loading rate from ring tests by Price and Knill [15].

fluctuations in strength at the higher rates. It will be shown that such behavior is consistent with the fourth hypothesis mentioned above.

To summarize, three different types of behavior have been observed with increasing rate of deformation: (1) either a constant strength or a constant rate of increase in strength, (2) a sudden increase in strength above a certain rate, and (3) apparent fluctuations in strength above a certain rate.

EXPERIMENTS

Apparatus

The apparatus (Fig. 5) is the same as that described by Logan and Handin [12]. Its design and operation are discussed in detail in that paper, but three features are of particular interest in the analysis of the results.

The first is the loading ram that provides the intermediate strain-rate capability. The ram is activated by dumping gas pressure from the lower side of the loading cylinder through a quick-acting valve. Helium is used because its low density and viscosity give the rapid flow necessary to achieve the high loading rates. The ram acts together with the dampening cylinder to give a constant loading rate as measured by the external force gage.

Also of concern is the aluminum yoke that couples the loading and compensating pistons. This yoke carries the load exerted by the confining pressure on the two pistons, so that the ram is not needed to support the force of the confining pressure on the loading piston. When the ram loads the specimen, the yoke is free to move, and the compensating piston moves out of the vessel as the loading piston moves in, thus maintaining a constant volume in the vessel.

The third feature of interest is the controlled-clearance packing. The pressure in this system in controlled independently so that is can be adjusted to provide a minimum friction between the packing gland and the piston. This frictional force is measured before each test.

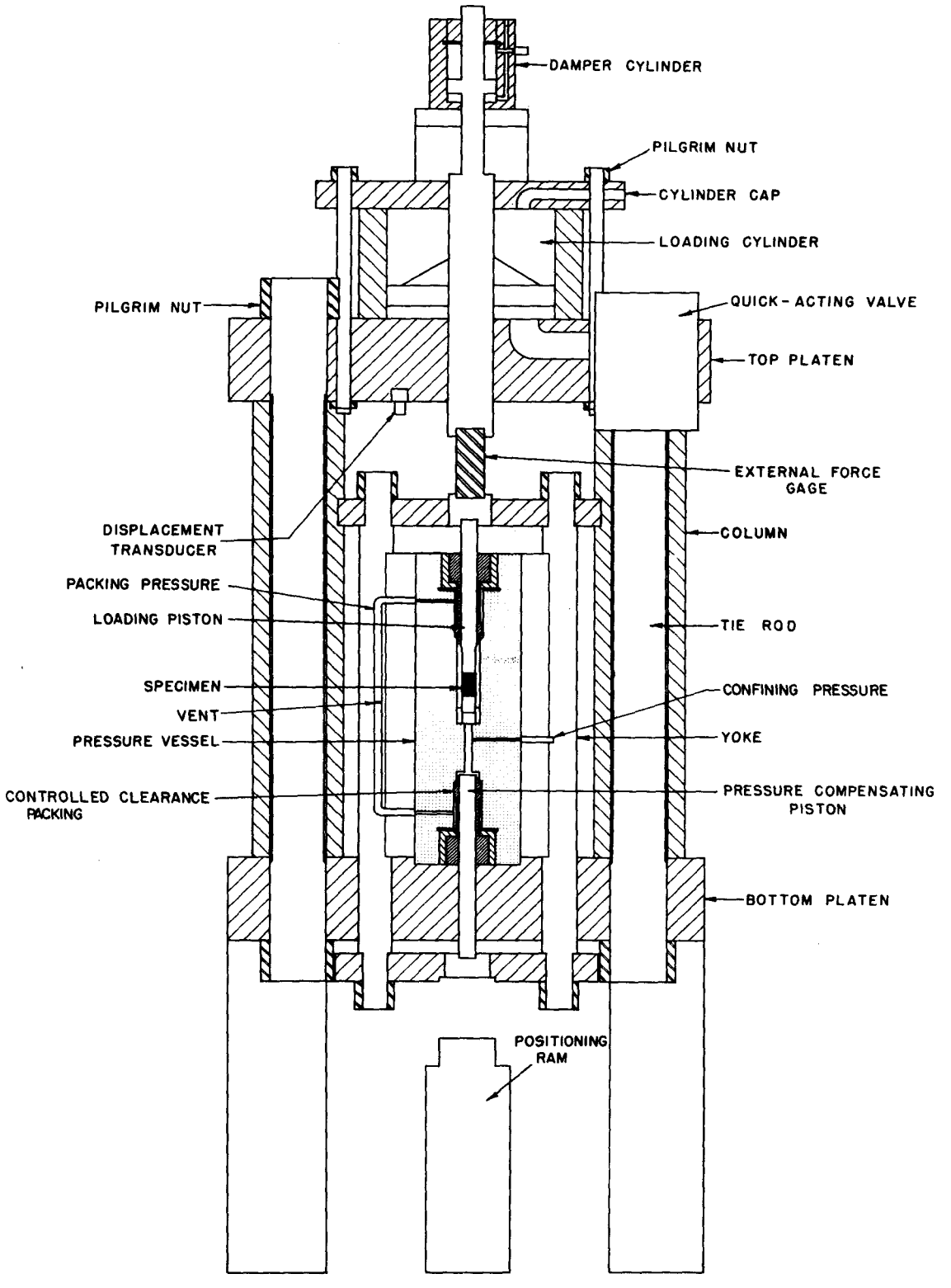

Figure 5. Schematic drawing of intermediate strain-rate apparatus. For scale, bottom platten is 15 cm thick (after Logan and Handin [27]).

In building up the confining pressure, the specimen is lifted off its seat 1 to 2 mm. Before the test, a regulating valve on the loading ram is used slowly to reseat the specimen. The force measured during this free travel is the frictional force on the pistons. For confining pressures below about 0.1 GPa, this force is too small to be measured by the force gage. For confining pressures of 0.25 and 0.45 GPa the frictional forces are not greater than 0.02 and 0.03 MN, respectively.

Rocks

The three rock types investigated are part of a standard rock suite for rapid excavation selected by the Bureau of Mines [9] (Table 2). These rocks represent three major catagories of failure processes: brittle fracture, cataclasis, and intracrystalline gliding.* The Charcoal Granodiorite is typical of crystalline, igneous rocks that have been shown to fail by brittle fracture at least to 0.5 GPa confining pressure and 500°C [2]. The Berea Sandstone is representative of clastic rocks that can deform by cataclastic flow. The Indiana Limestone represents carbonate sedimentary rocks that can deform by intracrystalline gliding as well as cataclasis.

A "dogbone" specimen-configuration is used to achieve more homogeneous end conditions (Fig. 6). In preliminary tests with straight cylinders, the deformation tended to be concentrated at the ends. The "dogbone" geometry produced more consistent results with deformation

*A fourth category, recrystallization flow, does not occur at the test conditions of this study.

Table 2. Description and properties of three rocks used in this study.*

				Porosity (percent)	Density g/cm^3	Dynamic Young's Modulus (GPa)	Compressive Strength (GPa)
Charcoal (St. Cloud Gray) Granodiorite	Quartz Microcline Plagioclase Biotite-Chlorite Hornblende Magnetite Rutile-appatite	16.7 20.0 40.8 9.5 11.7 1.2 0.1	medium-grained crystalline	0.08 ±0.05	2.72 ±0.003	48.4 ±4.9	0.282 ±0.006
Berea Sandstone	Quartz Feldspar Kaolinite Muscovite Carbonates	77.5 16.0 5.0 0.5 0.5	medium-grained clastic	19.1 ±0.5	2.11 ±0.01	8.5 ±0.8	0.046 ±0.004
Indiana (Salem) Limestone	Fossilferous calcite Calcite cement	69.0 31.0	medium-grained bioclastic	12.5 ±0.6	2.34 ±0.005	37.9 ±0.8	0.044 ±0.009

*Data from Bureau of Mines report, "A standard rock suite for rapid excavation research" (Krech et al. [9]).

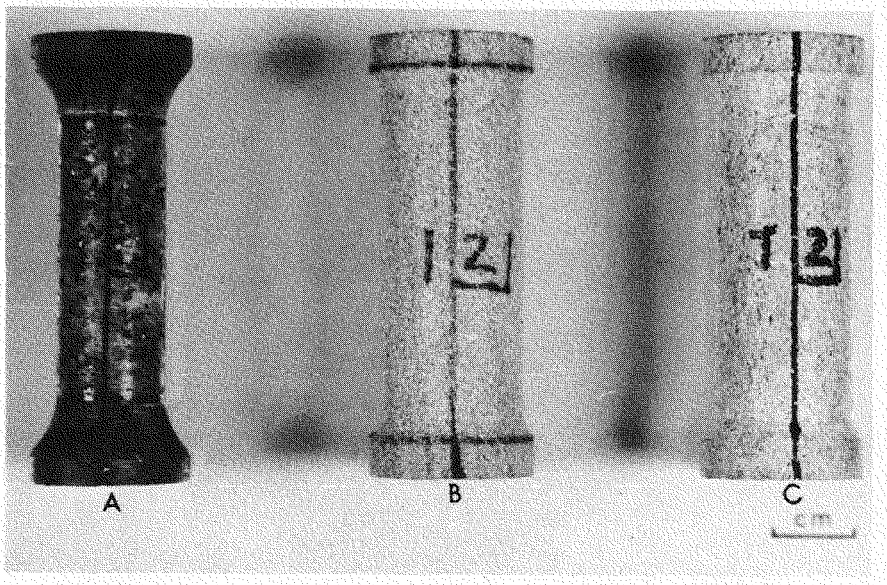

Figure 6. Undeformed "dogbone" specimens of Charcoal Granodiorite (A), Berea Sandstone (B), and Indiana Limestone (C). Epoxy fillets are used for the Charcoal Granodiorite, because of the difficulty in grinding this rock.

occuring away from the ends. This shape is produced by grinding the rocks with an 80 grit wheel while they are turned in a lathe. The ends of each specimen were surface-ground and lapped with 400-grit, silicon-carbide powder to within 0.075° of parallel.

Measurements

During each test force and displacement are measured externally to the pressure vessel (see Fig. 5, p. 11). Records are made on two storage oscilloscopes, one plotting force versus displacement and the other plotting force and displacement versus time.

The material property most frequently measured in previous work is "strength." In most of these studies the specimens were unconfined, and the rocks failed by brittle fracture. Thus there was little problem with the definition of strength. Because of the variety of behavior encountered in this study, however, it is necessary to define more precisely just what is measured in the different tests.

The phenomenon of concern is macroscopic failure, which is taken to mean the onset of permanent deformation on the scale of the specimen. This cannot be exactly determined from the records, so that a practical criterion must be decided upon for each type of result. The following definitions are used: (1) For specimens that fail by brittle fracture (total loss of load bearing capacity) or that work-soften after reaching a maximum load, the failure point is taken at the highest load achieved during the test (Figs. 7 and 8, all tests except 119, 141, and 147). (2) For those tests in which the stress-strain curve has a well-defined "knee", the failure point is taken at the

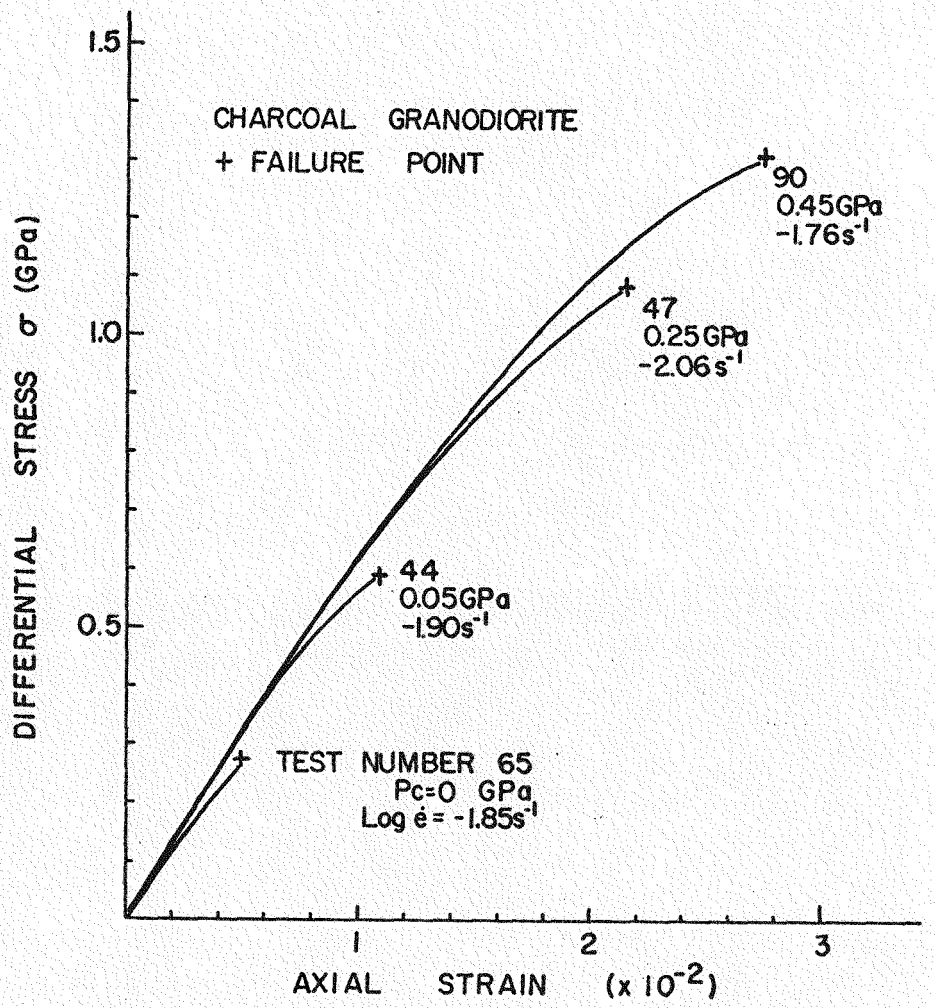

Figure 7. Representative stress-strain curves for Charcoal Granodiorite.

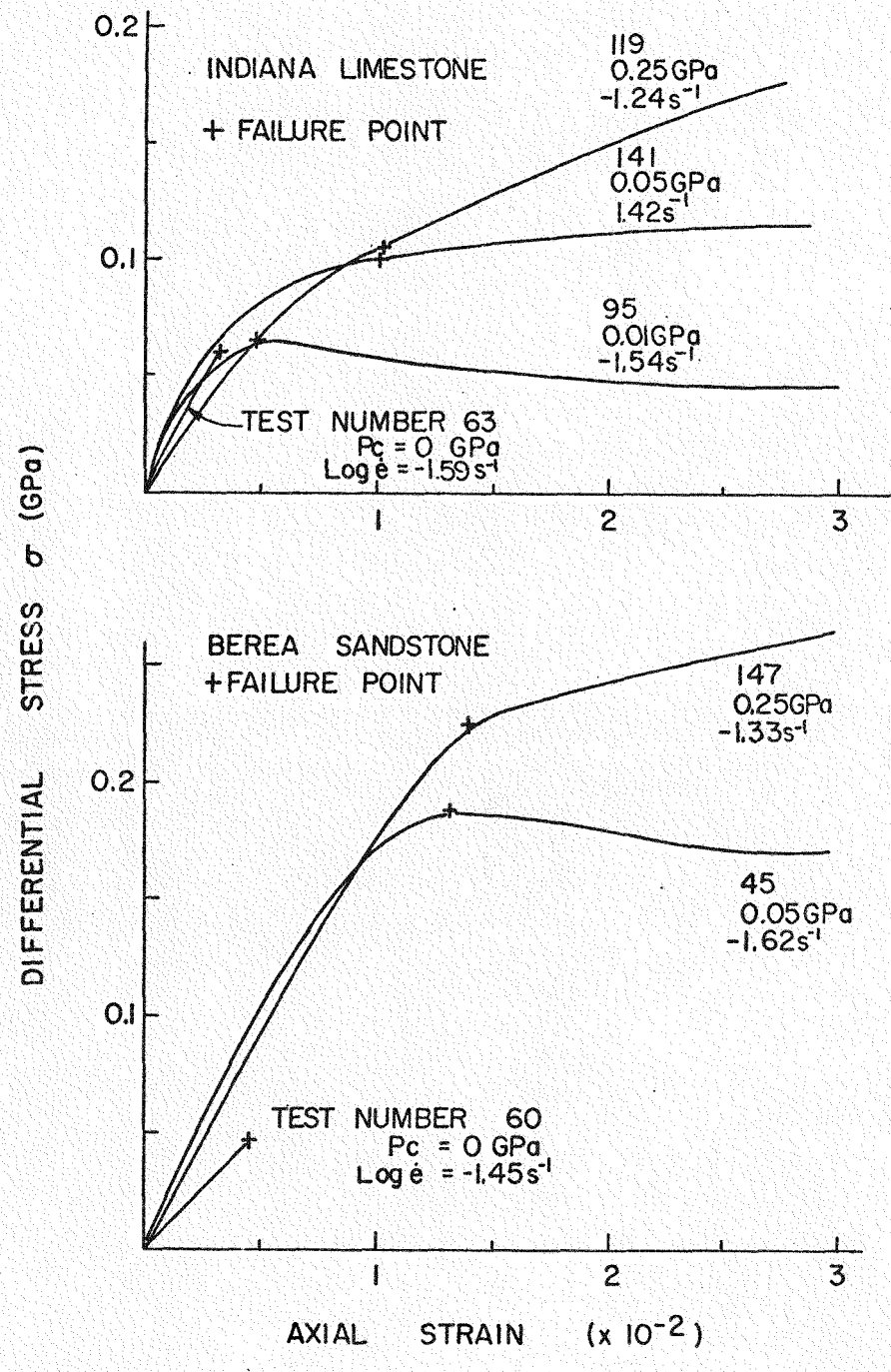

Figure 8. Representative stress-strain curves for Indiana Limestone and Berea Sandstone.

mid-point of the knee (Fig. 8, p. 17, test 147). In tests on the Indiana Limestone at 0.05 and 0.25 GPa confining pressure, no well-defined break occurs in the stress-strain curves. For the purpose of comparing "failure stresses" among tests on this rock, the failure point is taken at a strain of 0.01 (Fig. 8, p. 17, tests 119 and 141).

Two measurements, strain and apparent differential stress, are recorded at the failure point of each test. The strain is not a total axial strain in that it does not include the shortening of the specimen due to application of confining pressure alone. The differential stress is referred to as "apparent" because, as will be seen in later discussion, the axial force used to calculate this stress may contain inertial and dampening forces as well as the load carried by the specimen. The strain rate given for each test is an average value (see Appendix A).

Results

Room-temperature compression tests at strain rates from 10^{-2} to 10 s^{-1} were made on Charcoal Granodiorite to 0.45 GPa confining pressure and on Berea Sandstone and Indiana Limestone to 0.25 GPa confining pressure. The results are presented in Tables 3-5 and in Figs. 9-11. For each rock at each confining pressure, the apparent differential stress at failure is relatively constant up to a strain rate of about 1 s^{-1} and increases rapidly above this strain rate. The stresses for the unconfined tests at the slowest strain rates in this study fall within the margin of error of the compressive strengths given by the Bureau of Mines [9] (Table 2, p. 13). The strains at failure

Table 3. Summary of experiments on Charcoal Granodiorite

Test No.	Confining Pressure (GPa ±.0005)	Log Average Strain Rate (s^{-1})	Strain at Failure ($\times 10^{-2}$)	Apparent Differential Stress at Failure (GPa)
		±0.03	±0.03	±0.007
65	0	-1.85	0.50	0.276
64	0	-1.77	0.53	0.286
78	0	-1.20	0.47	0.286
127	0	-0.71	0.53	0.296
132	0	-0.07	0.59	0.296
58	0	0.31	0.45	0.317
66	0	0.34	0.32	0.368
59	0	0.36	0.53	0.348
80	0	0.44	0.37	0.409
		±0.02	±0.04	±0.01
44	0.05	-1.90	1.09	0.59
17	0.05	-1.88	1.10	0.56
135	0.05	-1.23	1.18	0.55
126	0.05	-0.65	1.22	0.56
10	0.05	-0.02	1.05	0.59
20	0.05	0.41	1.18	0.56
21	0.05	0.46	1.26	0.67
22	0.05	0.54	1.33	0.84
48	0.05	0.56	1.11	0.84
		±0.02	±0.06	±0.02
148	0.25	-2.12	2.13	1.02
47	0.25	-2.06	2.16	1.08
134	0.25	-1.44	2.05	1.02
125	0.25	-0.45	2.26	1.00
131	0.25	0.18	2.02	1.00

Table 3 (continued)

Test No.	Confining Pressure (GPa ±.0005)	Log Average Strain Rate (s^{-1})	Strain at Failure ($X10^{-2}$)	Apparent Differential Stress at Failure (GPa)
186	0.25	0.57	2.26	1.08
130	0.25	0.71	2.03	1.27
		±0.02	±0.07	±0.02
16	0.45	-1.80	2.46	1.27
90	0.45	-1.76	2.77	1.31
123	0.45	-1.09	2.63	1.25
124	0.45	0.47	2.70	1.25
171	0.45	0.19	2.78	1.35
128	0.45	0.52	2.70	1.27
82	0.45	0.78	2.77	1.37

Table 4. Summary of experiments on Berea Sandstone

Test No.	Confining Pressure (GPa ±.0005)	Log Average Strain Rate (s^{-1})	Strain at Failure ($\times 10^{-2}$)	Apparent Differential Stress at Failure (GPa)
		±0.03	±0.02	±0.004
60	0	-1.45	0.46	0.047
61	0	-1.43	0.52	0.047
77	0	-0.78	0.45	0.053
76	0	-0.19	0.43	0.065
72	0	0.28	0.32	0.077
70	0	0.30	0.37	0.083
56	0	0.37	0.40	0.007
57	0	0.37	0.44	0.012
69	0	0.44*	0.18	0.095
68	0	0.47	0.28	0.118
		±0.02	±0.05	±0.004
45	0.05	-1.62	1.32	0.189
29	0.05	-1.60	1.25	0.184
138	0.05	-0.95	1.23	0.184
152	0.05	-0.34	1.25	0.184
162	0.05	0.12	1.25	0.225
42	0.05	0.52	1.32	0.255
43	0.05	0.58	1.31	0.260
27	0.05	0.74	1.20	0.308
		±0.02	±0.06	±0.005
93	0.0625	-1.60	1.46	0.201
92	0.0750**	-1.59	1.51	0.213
108	0.0865**	-1.64	1.68	0.237
91	0.10**	-1.61	1.82	0.249

Table 4 (continued)

Test No.	Confining Pressure (GPa, ±.0005)	Log Average Strain Rate (s^{-1})	Strain at Failure ($X10^{-2}$)	Apparent Differential Stress at Failure (GPa)
149	0.0875	-0.40	1.54	0.231
151	0.1000**	-0.35	1.66	0.249
169	0.0625	0.60	1.66	0.337
106	0.0750	0.58	1.52	0.326
103	0.0875	0.62	1.65	0.332
104	0.0875	0.64	1.84	0.332
101	0.1000**	0.52	1.66	0.343
146	0.25**	-1.74	1.44	0.237
147	0.25**	-1.33	1.40	0.225
137	0.25**	-1.02	1.31	0.219
150	0.25**	-0.36	1.41	0.123
163	0.25**	0.42	1.56	0.266
164	0.25**	0.58	1.30	0.320

*±0.05

**Cataclastic flow, otherwise specimen contains shear fracture.

Table 5. Summary of experiments on Indiana Limestone

Test No.	Confining Pressure (GPa, ±.0005)	Log Average Strain Rate (s^{-1})	Strain at Failure ($X10^{-2}$)	Apparent Differential Stress at Failure (GPa)
		±0.04	±0.02	±0.004
63	0	-1.59	0.33	0.059
62	0	-1.54	0.34	0.053
139	0	-0.91	0.36	0.053
73	0	-0.26	0.35	0.059
74	0	-0.11	0.39	0.059
71	0	0.16	0.25	0.071
52	0	0.19	0.25	0.083
53	0	0.19	0.25	0.101
54	0	0.24	0.28	0.089
67	0	0.24	0.22	0.130
79*	0	-0.97	0.36	0.059
75*	0	-0.25	0.50	0.083
161*	0	-0.09†	0.24††	0.065
55*	0	0.05	0.25	0.142
		±0.05	±0.05	±0.004
97	0.005	-1.57	0.47	0.071
118	0.005	-1.27	0.48	0.065
95	0.010	-1.54	0.48	0.065
112	0.015#	-1.66	0.46	0.077
94	0.020#	-1.58	0.55	0.083
155	0.020	-0.39	0.61	0.095
156	0.025#	-0.34	0.78	0.101

Table 5 (continued)

Test No.	Confining Pressure (GPa, ±.0005	Log Average Strain Rate (s^{-1})	Strain at Failure ($X10^{-2}$)	Apparatus Differential Stress at Failure (GPa)
117	0.005	0.29**	0.34	0.160
116	0.015	0.46##	0.38	0.148
115	0.020	0.49	0.62	0.166
170	0.025#	0.52	0.76	0.178
		±0.04	±0.05	±0.004
141	0.05#	-1.42	1.02	0.101
142	0.05#	-1.42	1.02	0.107
140	0.05#	-0.83	1.03	0.095
154	0.05#	-0.24	1.04	0.101
160	0.05#	0.28	1.05	0.136
166	0.05#	0.50	1.04	0.201
		±0.03	±0.05	±0.004
143	0.25#	-1.29	1.06	0.107
119	0.25#	-1.24	1.03	0.107
136	0.25#	-0.82	1.05	0.107
153	0.25#	-0.28	1.03	0.124
157	0.25#	0.29	1.06	0.136
165	0.25	0.50	1.04	0.207

* with yoke

\# Ductile, otherwise specimen contains shear fracture

† ±0.10

** ±0.07

±0.06

†† ±0.05

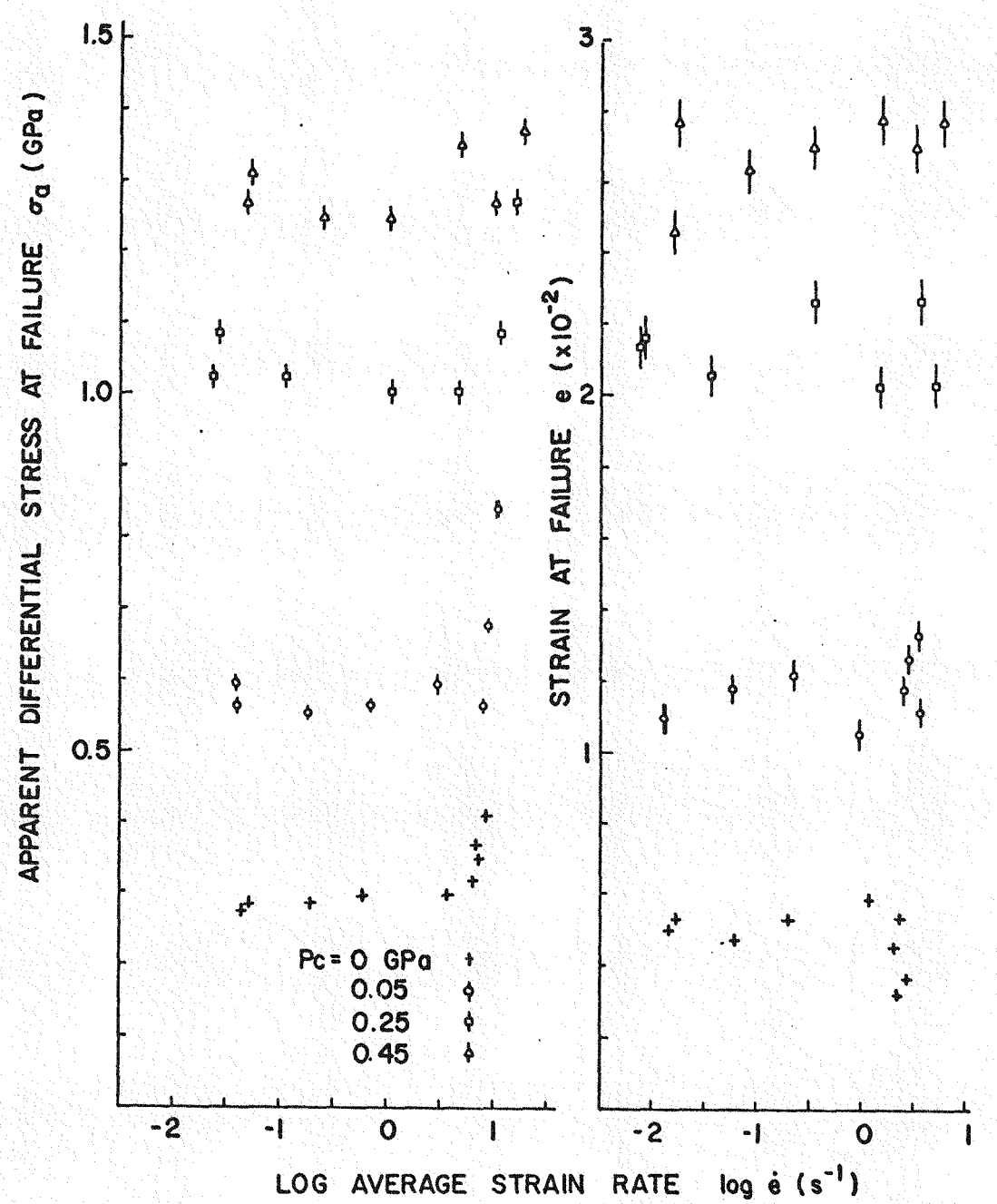

Figure 9. Strain-rate dependence of apparent differential stress and strain at failure for Charcoal Granodiorite.

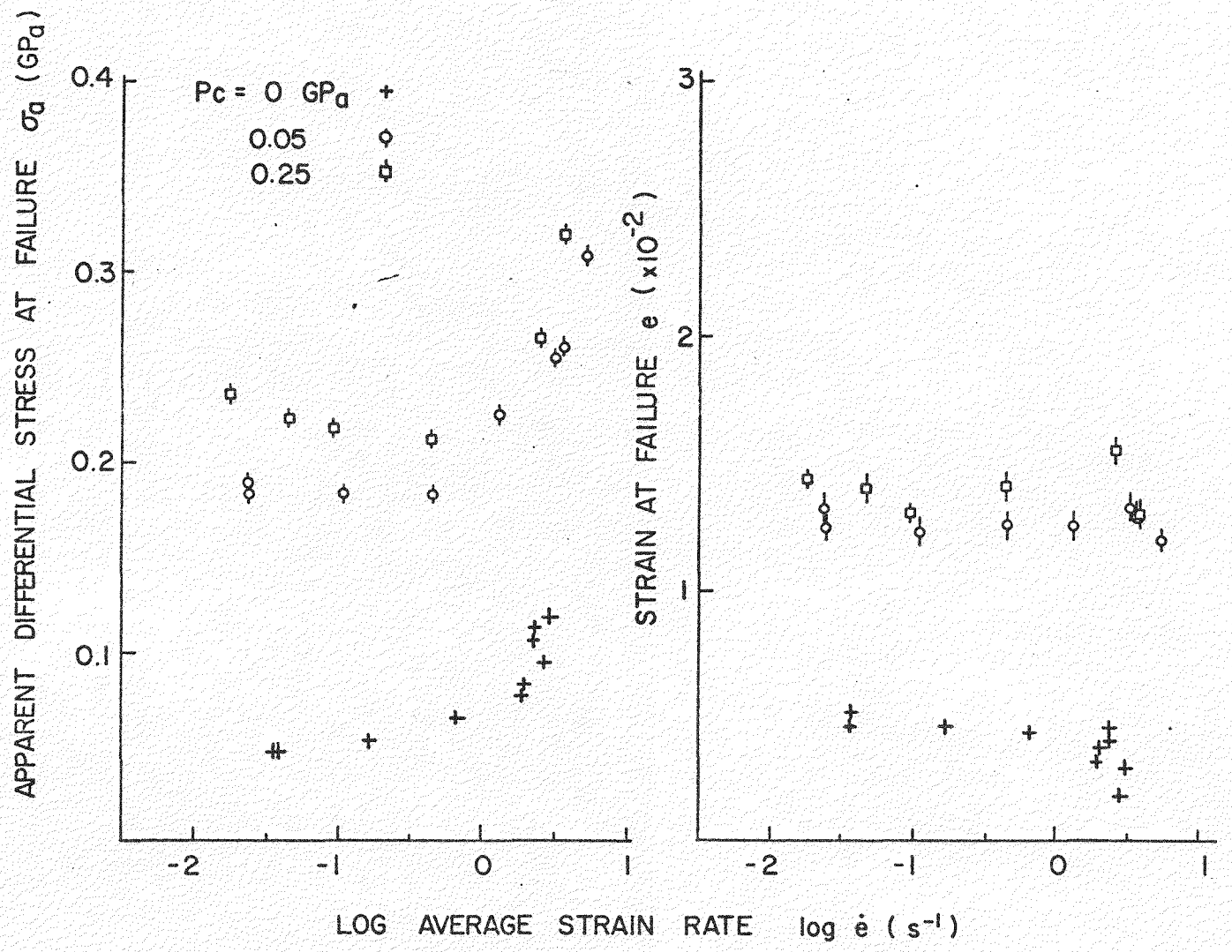

Figure 10. Strain-rate dependence of apparent differential stress and strain at failure for Berea Sandstone.

Figure 11. Strain-rate dependence of apparent differential stress and strain at failure for Indiana Limestone.

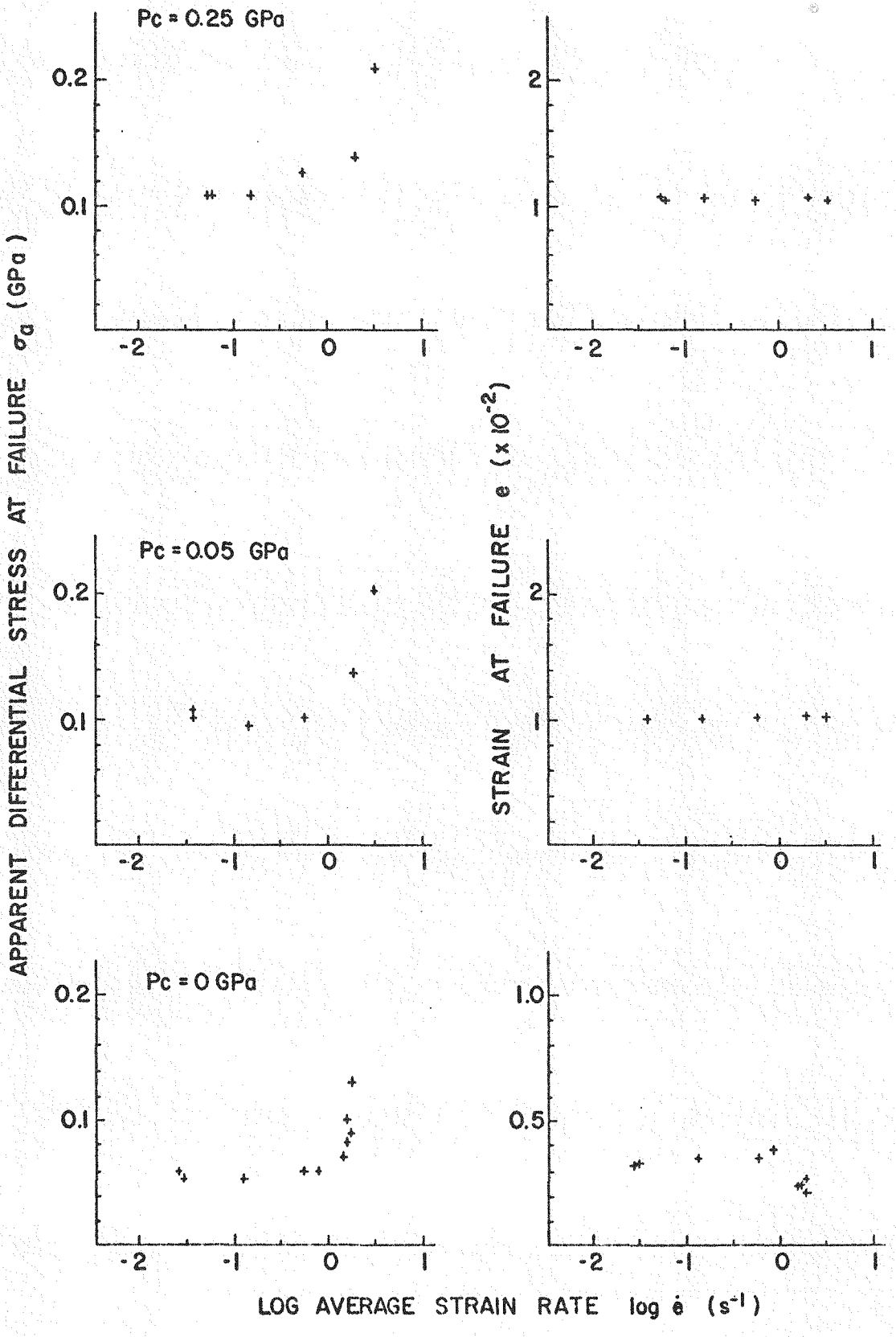
Pc = 0.25 GPa
Pc = 0.05 GPa
Pc = 0 GPa
APPARENT DIFFERENTIAL STRESS AT FAILURE σ_a (GPa)
STRAIN AT FAILURE e ($\times 10^{-2}$)
LOG AVERAGE STRAIN RATE log $\dot{e}$ (s^{-1})
0.2
0.1
2
1
1.0
0.5
-2
-1
0
1

are relatively insensitive to changes in strain rate except for the unconfined tests where they begin to decrease above a strain rate of about 1 s^{-1}.

An additional observation made for each test is the mode of failure. The Charcoal Granodiorite is brittle under all test conditions. With increasing confining pressure the Berea Sandstone and the Indiana Limestone pass from brittle to ductile behavior in three stages: (1) brittle fracture where the specimen loses cohesion (Fig. 7, p. 16; Fig. 8, p. 17, tests 60 and 63), (2) ductile fracture or faulting where most of the shortening occurs as displacement on a shear fracture without loss of cohesion (Fig. 8, p. 17, tests 45 and 95; Fig. 12, tests 42, 45, 99, 104, 106), and (3) ductile behavior where there is no loss of cohesion and deformation is pervasive (Fig. 8, p. 17, tests 119, 141, 147; Fig. 12, tests 91, 101, 108). With increasing strain rate the Berea Sandstone and Indiana Limestone become more brittle. At a strain rate of 2.5×10^{-2} s^{-1} the Berea Sandstone enters the third stage of the transition at a confining pressure of about 75 MPa, whereas at a strain rate of 4.0 s^{-1} it enters this stage at about 100 MPa (Fig. 12). The transition in the Indiana Limestone occurs at a lower confining pressure and is not quite as sensitive to changes in strain rate. It shifts from a confining pressure of 15 MPa at a strain rate of 2.5×10^{-2} s^{-1} to 25 MPa at 3.2 s^{-1} (see Table 5, p. 23).

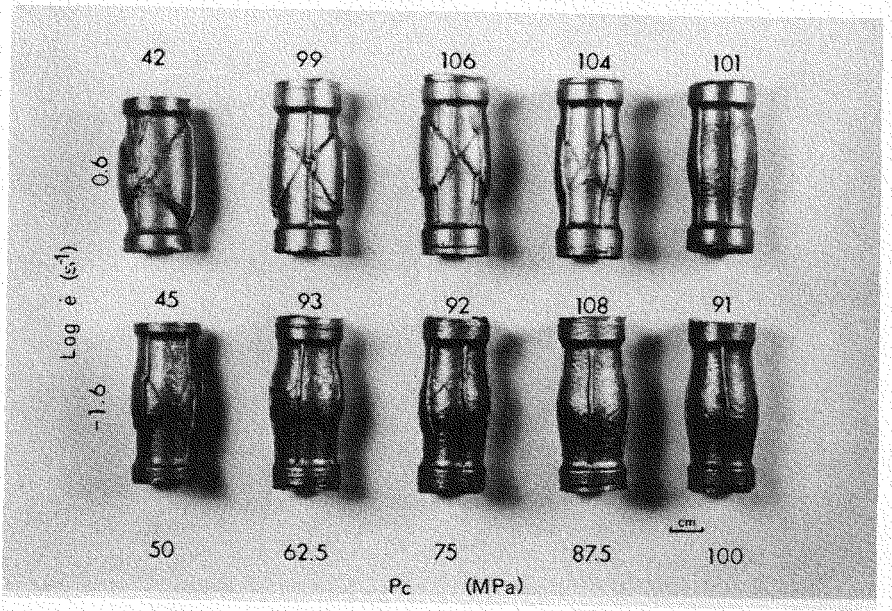

Figure 12. Effect of strain rate on the brittle-ductile transition in Berea Sandstone. Specimens are in lead jackets with test numbers indicated above each.

ANALYSIS

Stresses and strain rates reported for an experiment are not usually measured directly within the specimen but are calculated from force and displacement measurements made some distance from the specimen. At high strain rates it is possible that the calculated value for stress may contain inertial forces related to the loading frame and piston as well as the load carried by the specimen. The following analysis is undertaken to predict the effect of inertia on the measurements made during such tests. The procedure followed is to (1) write an equation of motion for a simple mechanical model of the apparatus; (2) given a force input and initial conditions for displacement, obtain a solution to this equation in the form of a displacement function; and (3) assign to the model a failure criterion based on the results of the experiments and use the theoretical force and displacement functions to calculate a strain and apparent failure stress as a function of strain rate for the model, just a they would be calculated from the measurements made during a test.

The mechanical model is shown in Fig. 13. The equation of motion for this system is

$$F(t) = \left(m \frac{d^2}{dt^2} + c \frac{d}{dt} + k\right) u(t) \qquad (1)$$

where

$F(t)$ = force

$u(t)$ = displacement

t = time

m = mass

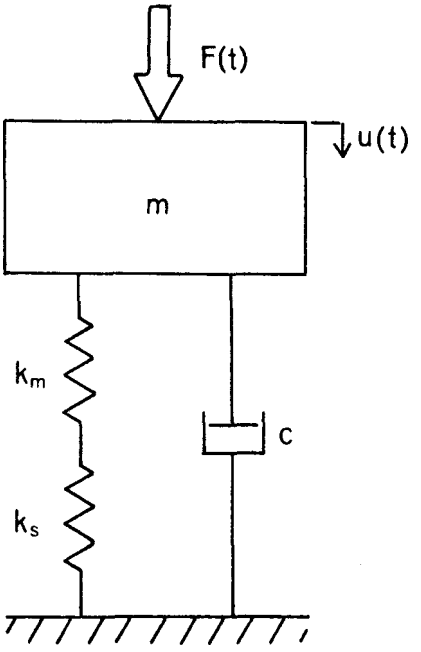

Figure 13. Mechanical model of the apparatus. F(t), force; u(t), displacement; m, mass; c, dampening coefficient; k_m, machine stiffness; k_s specimen stiffness.

$c \equiv$ dampening coefficient

$k_m \equiv$ machine stiffness

$k_s \equiv$ specimen stiffness

$k \equiv \frac{k_m k_s}{k_m k_s}$, effective stiffness for elastic members in series.

In the experiments, the loading rate is constant, so the force function is taken as

$$F(t) - rt$$

where r is the loading rate. With initial conditions for a system at rest,

$$u(o) = \frac{du}{dt}\Big|_{t=o} = \frac{d^2u}{dt^2}\Big|_{t=o} = 0$$

the Laplace transform method can be used to obtain the following solution to equation 1 (see Appendix B),

$$u(t) = \frac{r}{k}\{t - \frac{c}{k}[1 - \exp(-at)(\cos bt + \frac{a^2 - b^2}{2ab} \sin bt)]\} \qquad (2)$$

where

$$a \equiv \frac{c}{2m}$$

$$b^2 \equiv \frac{k}{m} - (\frac{c}{2m})^2$$

Some examples of u(t) for different loading rates are shown in Fig. 14. The solution is compared with the experimental displacement-time records in Figs. 15 and 16. The dampening is expressed in terms of a decay time given by

$$t_o \equiv 1/a = 2m/c,$$

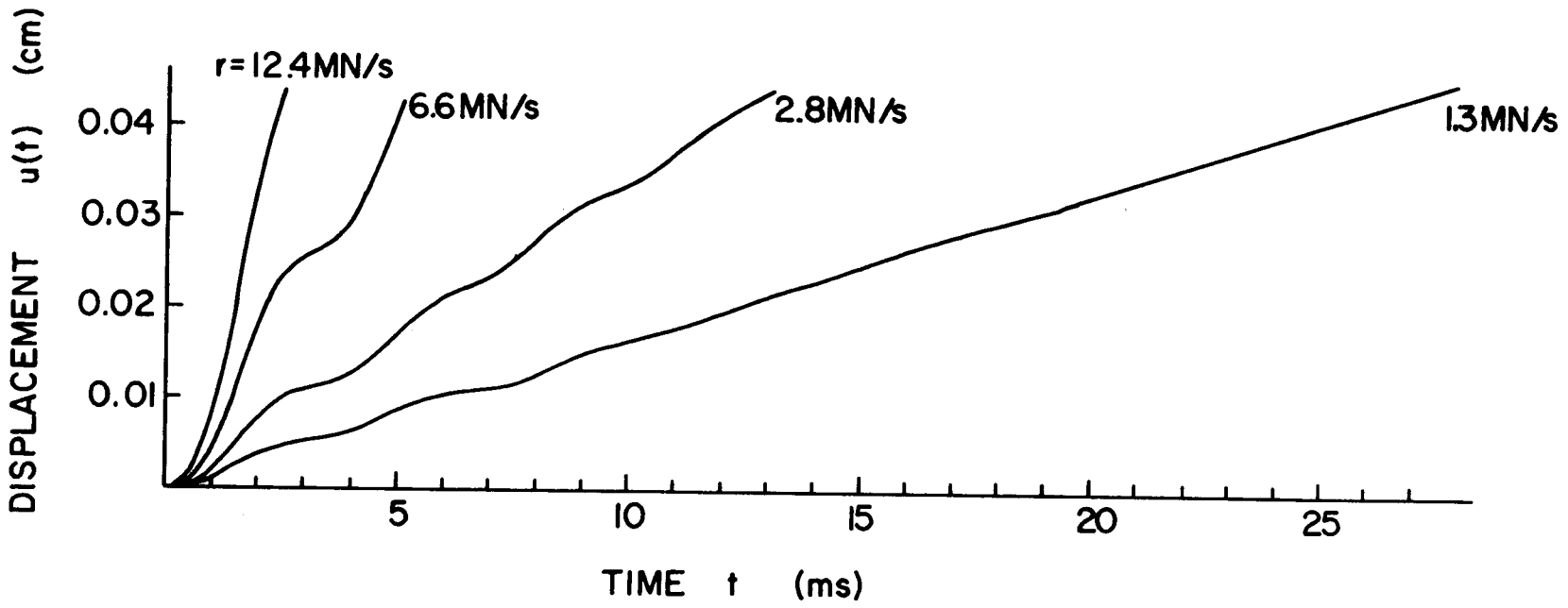

Figure 14. Theoretical displacement-time curves for different loading rates.

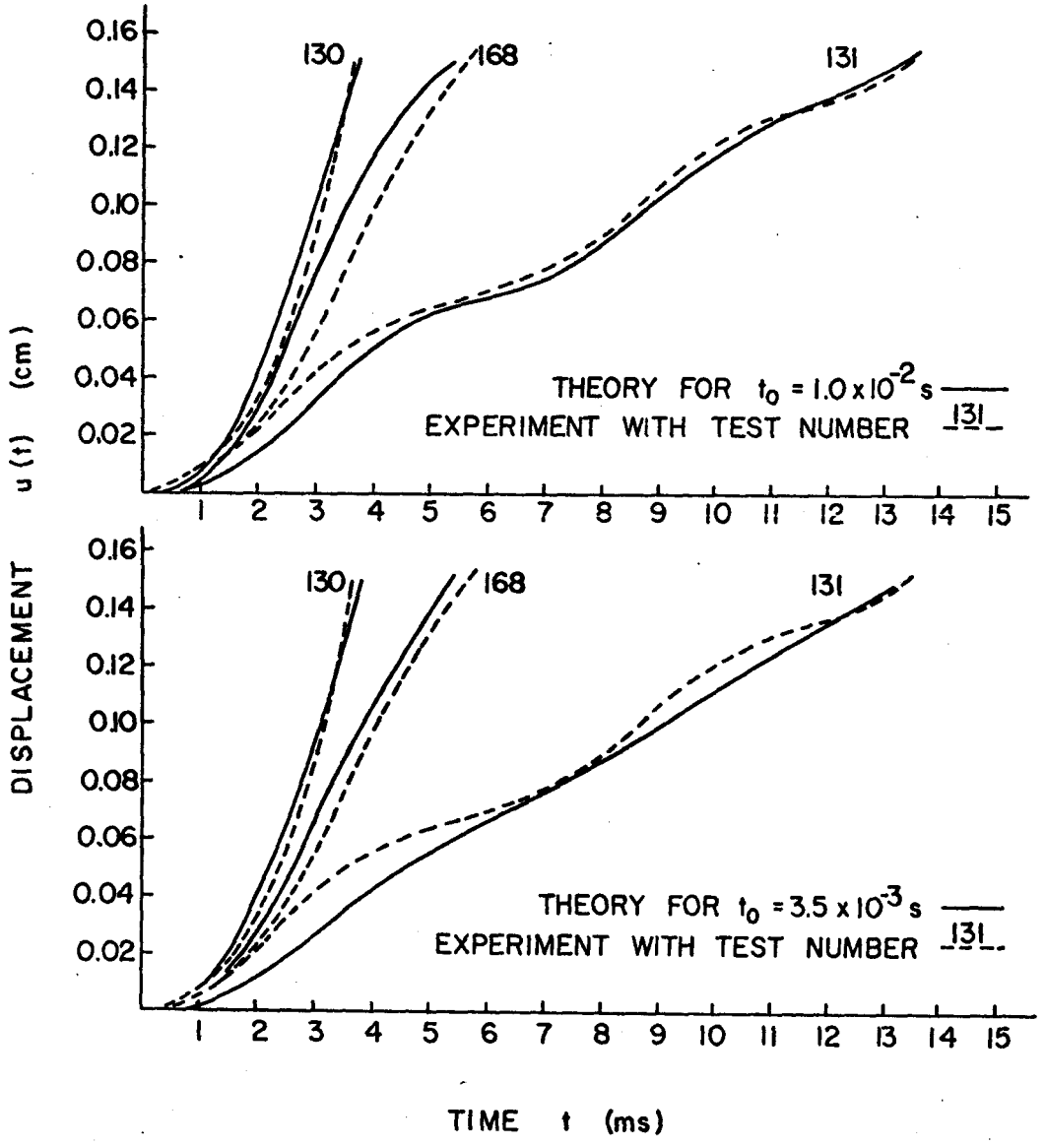

Figure 15. Displacement-time curves for experiments on Charcoal Granodiorite at 0.25 GPa confining pressure compared with theoretical curves for two different decay times.

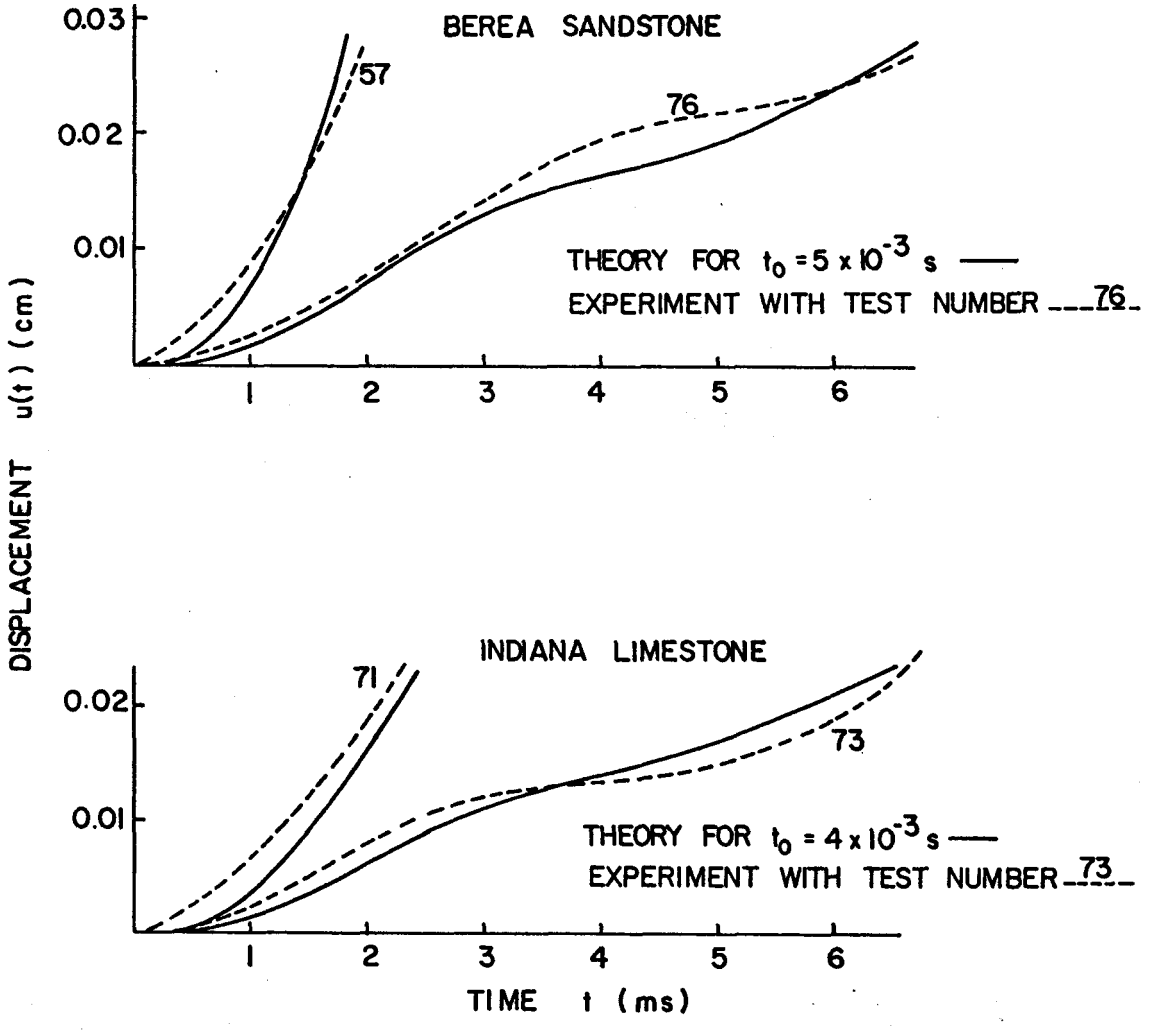

Figure 16. Displacement-time curves for unconfined experiments on Berea Sandstone and Indiana Limestone compared with theoretical curves.

which is the time taken for the amplitude of the wave to decay to exp (-1) its original value.

Two comments need to be made regarding the dashpot in Fig. 13 (p. 32). First, when the dashpot is put in series with the springs, the solution is a parabolic curve with a superimposed wave motion. This type of behavior was not observed in the experiments; therefore, the model in Fig. 13 (p. 30) is the best, simple model. Second, it should be emphasized that the dashpot in Fig. 13 (p. 30) is not meant to represent the dampening cylinder is Fig. 5 (p. 11). This cylinder is part of the system producing the input, F(t), to the model and not part of the model itself.

The inertial force is proportional to the acceleration, given by

$$\frac{d^2u}{dt^2} = \frac{r}{mb} \exp(-at) \sin bt \qquad (3)$$

At higher strain rates, this acceleration is amplified in two ways: first by the smaller t in the exponential term, and second by the higher loading rate, r, necessary to produce a higher strain rate.

To get an idea of the effect inertia can have on the results of a test, consider a comparison between an apparent stress at failure calculated directly from the measured force,

$$\sigma_a (t_1) \equiv F(t_1)/A \qquad (4)$$

where $t_1 \equiv$ time of failure

A = cross-sectional area of the specimen

and a failure stress whose calculation accounts for the inertial effect.

$$\sigma(t_1) \equiv [F(t_1) - m \left.\frac{d^2u}{dt^2}\right|_{t=t_1}]/A. \tag{5}$$

With the aid of equation 3, the following relation between the two stresses can be derived,

$$\sigma_a(t_1) = t_1\sigma(t_1)/[t_1 - \frac{1}{b} \exp(-at_1) \sin bt_1] \tag{6}$$

For large t_1, $\sigma_a \simeq \sigma$, but for the higher strain-rate tests in which t_1 becomes smaller, σ_a oscillates about σ, and finally for $o < t_1 < \pi/b$, σ_a increases monotonically above σ.

In order to apply this analysis to the experiments, two questions must be answered about the nature of σ as calculated by equation 5. Can it be regarded as a true failure stress? And does it vary with strain rate? The first question depends on whether or not the term $c \frac{du}{dt}$ in equation 1 represents rock or machine behavior. For a first approximation, it is assumed to represent rock behavior, and σ as calculated by equation 5 is regarded as the true failure stress. As for the second question, the experimental data show that for low strain rates the failure stress is relatively independent of strain rate, so for a first approximation σ will be taken as

$$\sigma(t_1) \equiv \sigma_1 \tag{7}$$

where σ_1 is a constant equal to an average of the failure stresses at the lower strain rates. This is henceforth referred to as the "stress criterion." The corresponding strains are given by

$$e(t_1) = \frac{A\,\sigma_1}{Lk_s\,(1 + \frac{cq}{kp})} \tag{8}$$

where $L \equiv$ specimen length

$$p \equiv t_1 - \frac{c}{k}\left[1 - \exp(-at_1)\left(\cos bt_1 + \frac{a^2 - b^2}{2ab}\sin bt_1\right)\right]$$

$$q \equiv 1 - \exp(-at_1)\left(\cos bt_1 + \frac{a}{b}\sin bt_1\right)$$

To model the strains as they are actually calculated from the tests the following formula is used instead of equation 8,

$$e(t_1) \simeq \frac{A}{L}\,\sigma_1\left(\frac{1}{k + c\,\frac{q}{p}} - \frac{1}{k_m}\right) \tag{9}$$

(See Appendix B for the difference in equations 8 and 9.) The average strain rate is given by

$$\dot{e}(t_1) = e(t_1)/t_1 \tag{10}$$

Now with equations 6, 7, 9, and 10, curves can be plotted for apparent failure stress and strain versus log average strain rate (Fig. 17). This theory is applied to the results of the unconfined tests with a fair degree of success (Figs. 18-20).

The strains at failure for the tests run at confining pressure are relatively constant and do not show the behavior predicted by equations 8 or 9. In fact, for the tests on Indiana Limestone at 0.05 and 0.25 GPa confining pressure, the strains at failure are constant by definition. This suggests an alternate way of specifying the strain-rate dependence of a failure criterion for the model; that is, the strain at failure is independent of strain rate and is given by

$$e(t_1) \equiv e_1 \tag{11}$$

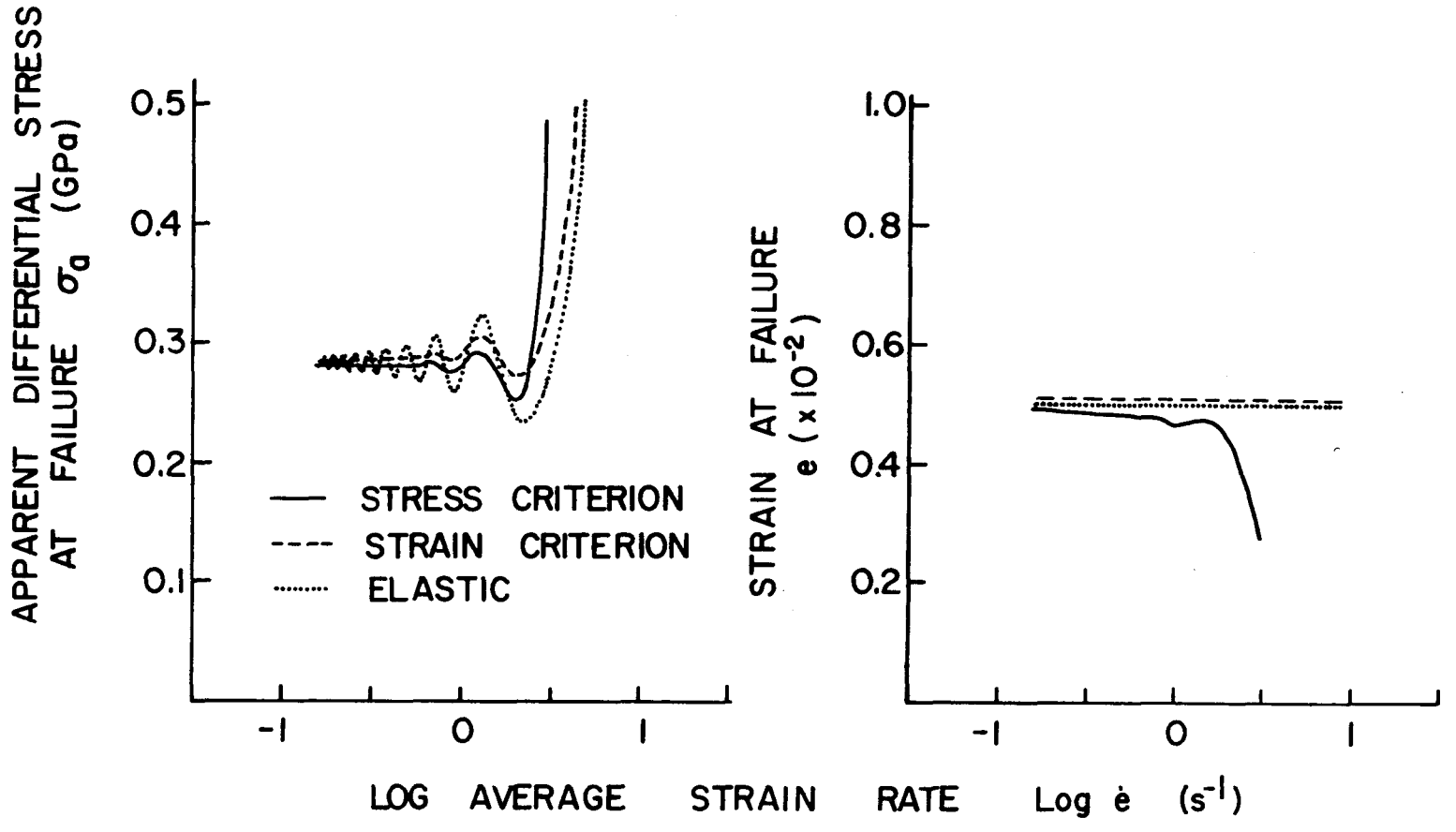

Figure 17. Theoretical strain-rate dependence of apparent stress and strain at failure.

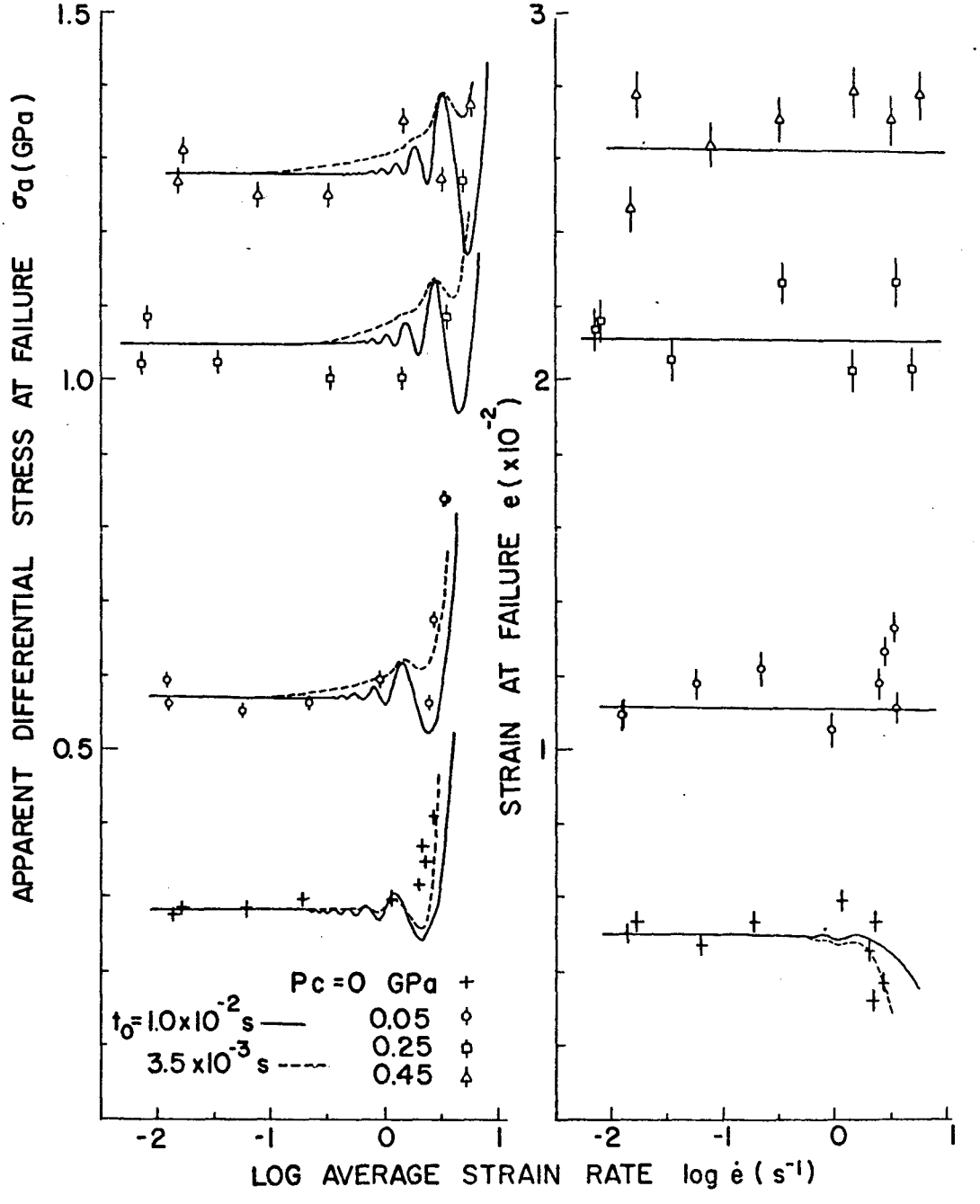

Figure 18. Comparison of theoretical and experimental strain-rate dependence of apparent differential stress and strain at failure for the Charcoal Granodiorite.

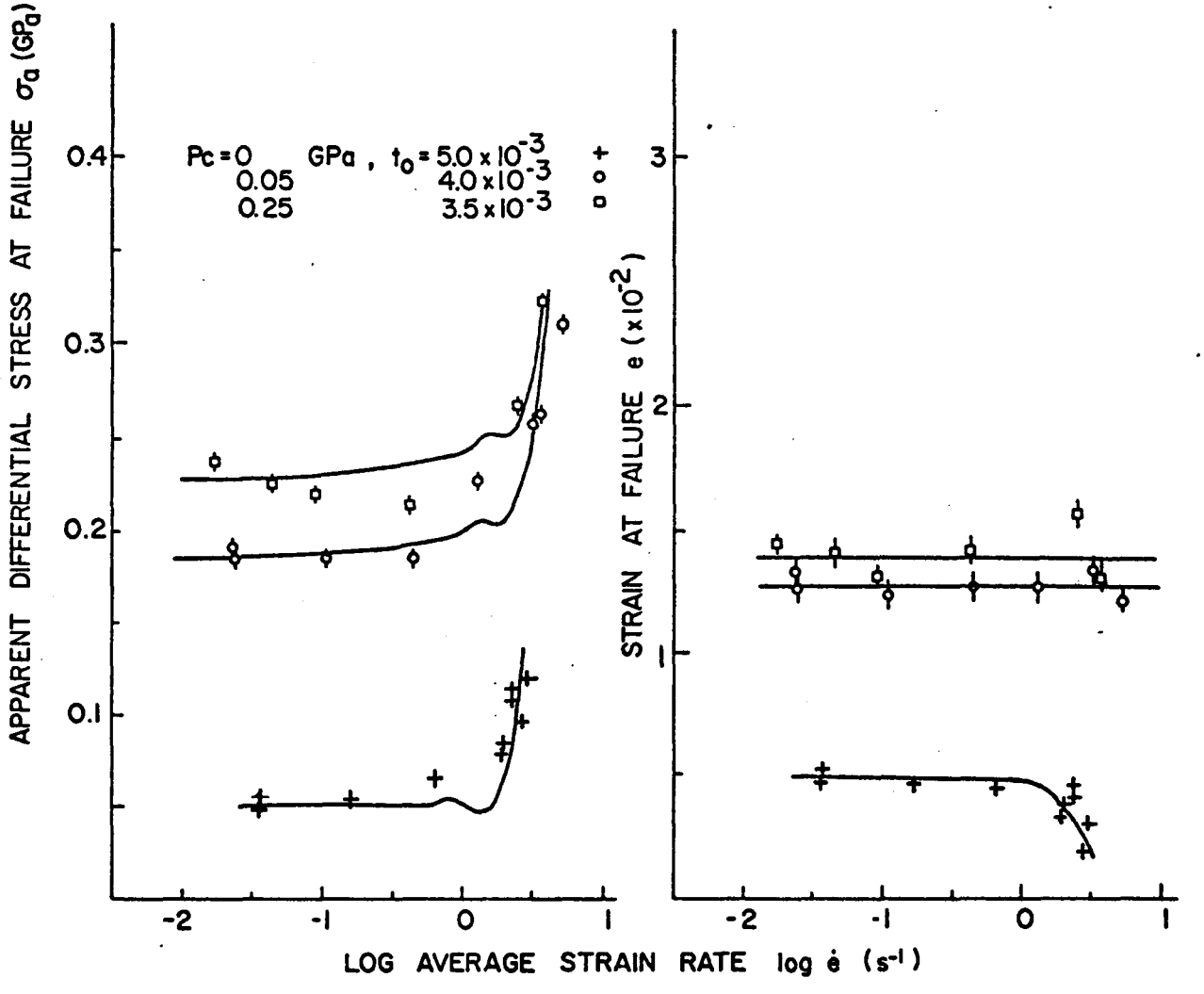

Figure 19. Comparison of theoretical and experimental strain-rate dependence of apparent differential stress and strain at failure for Berea Sandstone.

Figure 20. Comparison of theoretical and experimental strain-rate dependence of apparent differential stress and strain at failure for Indiana Limestone.

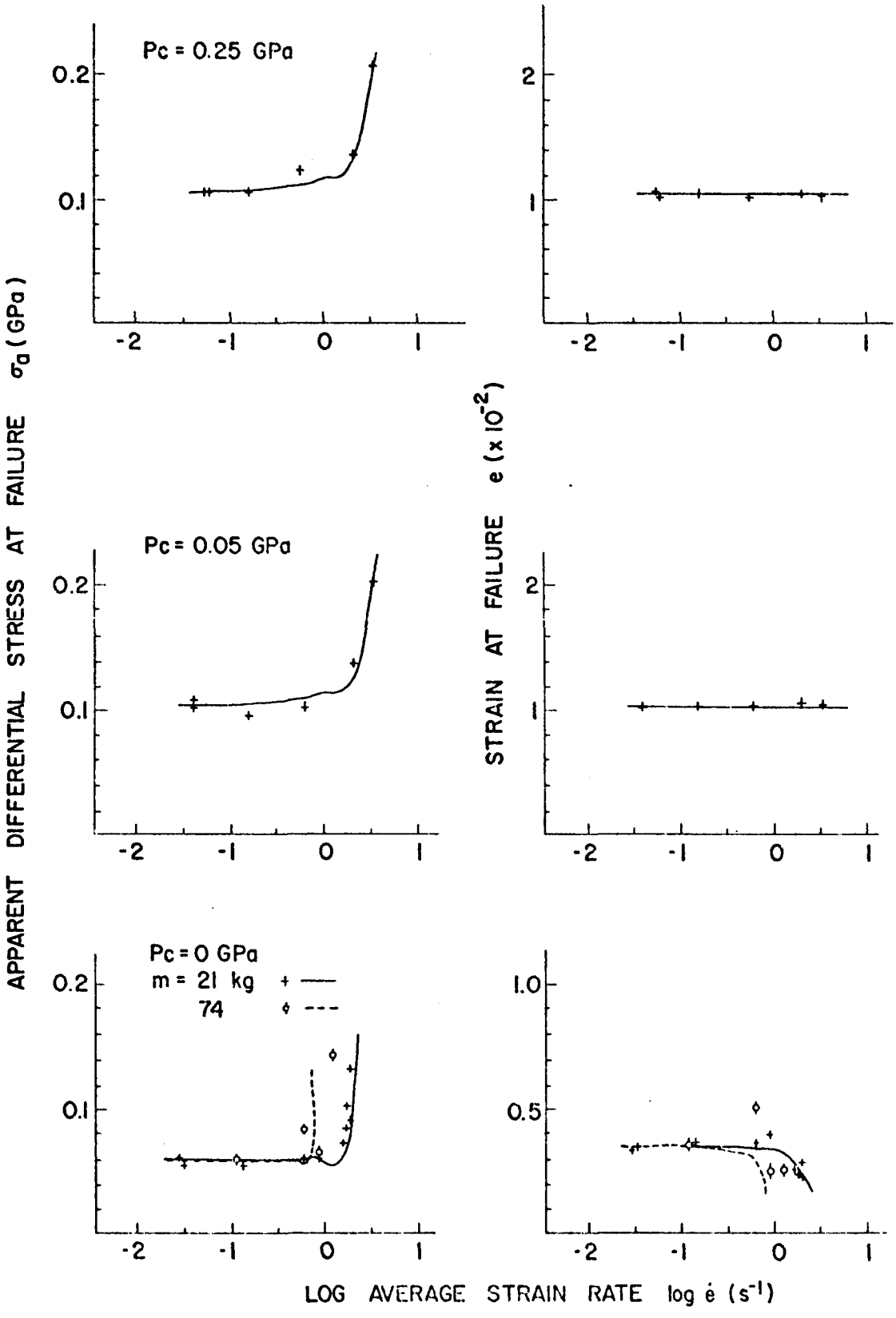
Pc = 0.25 GPa
Pc = 0.05 GPa
Pc = 0 GPa
m = 21 kg
74
APPARENT DIFFERENTIAL STRESS AT FAILURE σd (GPa)
STRAIN AT FAILURE e (x 10⁻²)
LOG AVERAGE STRAIN RATE log ė (s⁻¹)

where e_1 is the average measured strain at failure. This is referred to henceforth as the "strain criterion." The corresponding stress is given by

$$\sigma(t_1) = \frac{Lk_s}{A}\left(1 + \frac{cq}{kp}\right) e_1 \qquad (12)$$

From equations 6, 10, 11, and 12, the apparent stress and strain at failure can be plotted against the log of the average strain rate (Fig. 17, p. 40). This criterion is applied to the tests run at confining pressure in Figs. 18-20 (pp. 41-44).

The two questions must now be reconsidered with respect to the strain criterion. It is possible that the dampening term in equation 1 represents primarily machine response, particularly in the confining pressure tests, where there is considerable friction between the packing gland and the piston. If in the model the dampening term represents machine behavior, then the true stress at failure for the strain criterion is given by

$$\sigma_1 = \frac{Lk_s}{A} e_1 \qquad (13)$$

rather than by equation 12. If this is true then the answer to the second question is unchanged. The failure stress of the material is independent of strain rate for both the stress and the strain criterion. This interpretation offers an explanation of why the drop in failure strains at high strain rates occurs only in the unconfined tests.

In practice, both the machine and the specimen are contributing

to dampening. A more complex model would be required to separate the two effects and to determine which of them dominates. What is important here is that both criteria give similar curves for apparent stress plotted versus log average strain rate and that the overriding effect is that of the inertial term (Fig. 17, p. 40).

One suggestion for reducing the inertial effect would be to lower the mass involved either by reducing the mass of the yoke or by making measurements closer to the specimen. Theoretically, the effect of a change in mass is to shift the curve to the right an order of magnitude in strain rate for a two order-of-magnitude decrease in mass (Fig. 21). This shift has been tested in unconfined tests on Indiana Limestone (Fig. 20, p. 44). It is significant that relatively small masses still produce a sharp increase in apparent stress, the only difference being that the increase begins at a somewhat higher strain rate.

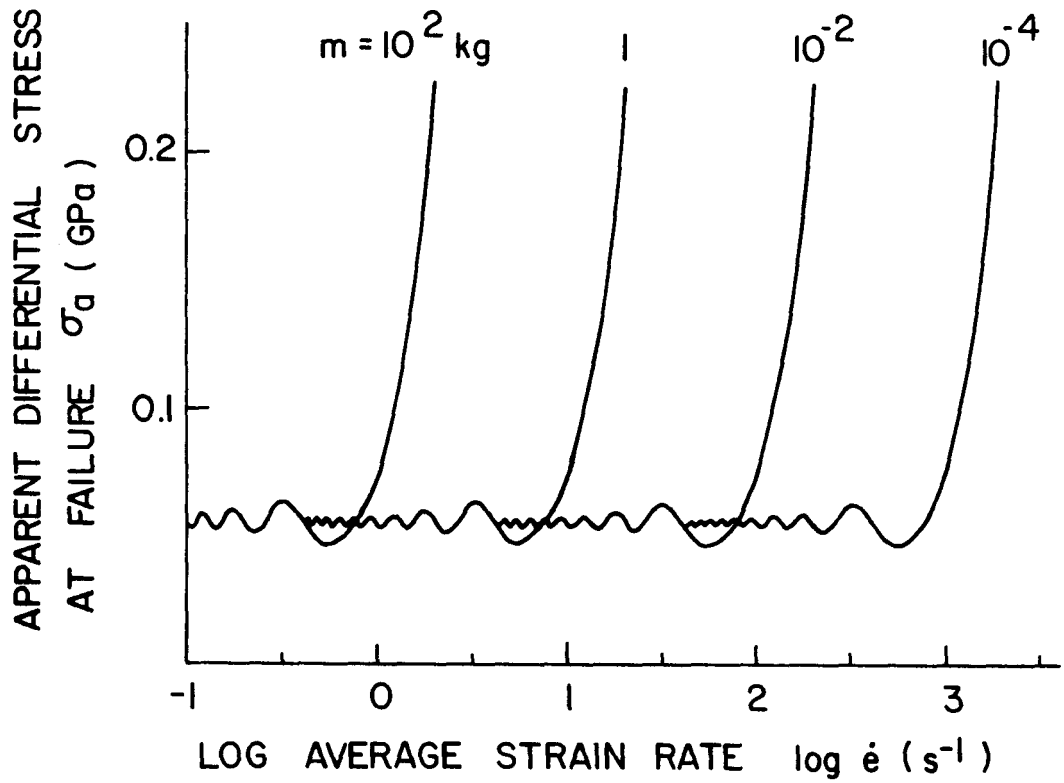

Figure 21. Effect of change in mass on plot of apparent stress at failure versus log average strain rate.

DISCUSSION

The three hypotheses proposed in earlier studies for strain-rate effects cannot explain the behavior observed in this study. In the first two hypotheses the critical strain rate at which the rapid increase in strength begins is theoretically related to the velocity of sound in the material. Kumar [10] relates the critical rate to the maximum crack-propagation velocity. In the three rocks tested in the present study a crack has time to propagate the length of the specimen 50 to 100 times during the tests in which an apparent increase in strength occurs (Appendix C). Thus the maximum crack propagation velocity cannot significantly limit the strain rate. In the second hypothesis the critical strain rate is supposed to have a value high enough to produce a state of uniaxial strain, but even in the fastest tests in the present study, a strain wave has time to travel from the boundary to the center of the specimen several hundred times (Appendix C), so that there is always more than enough time for the lateral strains to come to equilibrium, and a state of uniaxial strain cannot be achieved. The third hypohtesis calls on a change in the deformation mechanism. Several mechanisms are observed in this study, but the sudden increase in apparent failure stress occurs at about the same strain rate for each confining pressure for all three rocks, no matter how they deform.

The model developed in the previous section predicts (1) the critical strain rate at which the rapid increase in apparent stress begins and how steep the increase should be, (2) the effect of a

change in the mass of the loading system on the critical strain rate, and (3) the appearance of wave motion in the displacement-time records. In the model, the sudden increase in apparent failure stress can be directly attributed to inertia, thus the inertial effect affords the best explanation for the observed behavior.

Whether or not inertial forces have affected the results of other studies is an open question, the variety of testing devices and measuring techniques considered. However, this possibility should be given serious consideration because even small moving masses can produce a sharp increase in apparent failure stress similar to those reported by several previous workers [5, 8, 10, 13, 14, 20]. Also the inertial model is the only one treated here that predicts not only the increases in strength but also the fluctuations seen in at least two of the earlier studies [13, 15].

Atributing the variations in apparent failure stress to inertial effects in the machine leads to the conclusion that the true failure stress of the material is relatively independent of strain rate in the range from 10^{-2} to 10 s^{-1}. In the same interval there is a tendency for the strain necessary to fragment the rock to decrease with increasing strain rate. This effect is obvious in the unconfined tests for all three rocks. It is also suggested by the shift in the brittle-ductile transition in the Berea Sandstone and Indiana Limestone. The combination of relatively constant stress with decreasing strain at higher strain rates suggests that the energy necessary to break the rock may be lower at higher strain rates. To the engineer

interested in more rapid excavation of rock, a higher deformation rate may be advantageous from the point of view of both excavation rate and energy consumption.

CONCLUSIONS

1. The apparent sudden increase in failure stress agove a strain rate of about 1 s^{-1} is due to machine inertia and does not reflect a real increase in material strength.

2. The room-temperature failure stresses of the three rocks tested in this study are relatively insensitive to changes in strain rate between 10^{-2} and 10 s^{-1}.

3. The failure strains tend to decrease above a strain rate of about 1 s^{-1} for the unconfined tests for all three rocks. At confining pressure the failure strains remain relatively constant between 10^{-2} and 10 s^{-1}.

4. The two sedimentary rocks tend to be more brittle at the higher strain rates.

5. The energy necessary to fragment these rocks is either constant or tends to decrease with increasing strain rate.

REFERENCES

1. Birkimer D. L. A possible fracture criterion for the dynamic tensile strength of rock. Dynamic Rock Mechanics - Proc. Twelfth Symp. on Rock Mechanics (Ed. G. B. Clark), p. 573, AIME, New Yrok (1971).
2. Borg I. and Handin J. Experimental deformation of crystalline rocks. Tectonophysics 3, 249 (1966).
3. Brace W. F. and Jones A. H. Comparison of uniaxial deformation in shock and static loading of three rocks. J. Geophys. Res. 76, 4913 (1971).
4. Crittenden M. New data on the isostatic deformation of Lake Bonneville. U.S. Geol. Sur. Prof. Paper 454-E, 31 (1963).
5 Green S. J. and Perkins R. D. Uniaxial compression tests at strain rates from 10^{-4}/sec to 10^{4}/sec on three geological materials. Basic and Applied Rock Mechanics - Proc. Tenth Symp. on Rock Mechanics (Ed. K. E. Gray), p. 35, AIME, New York (1972).
6. Green S. J., Leasia J. D., Perkins R. D. and Jones A. H. Triaxial stress behavior of Solenhofen Limestone and Westerly Granite at high strain rates. J. Geophys. Res. 77, 3711 (1972).
7. Heard H. C. Effects of large changes in strain-rates in the experimental deformation of Yule Marble. J. Geol. 71, 162 (1963).
8. Kobayashi, R. On mechanical behaviors of rocks under various loading-rates. Rock Mech. in Japan 1, 56 (1970).
9. Krech W. W., Henderson F. A. and Hjelmstad K. E. A standard rock suite for rapid excavation research. Bureau of Mines Report of

Investigations 7865 (1974).

10. Kumar A. The effect of stress rate and temperature on the strength of basalt and granite. Geophysics 33, 501 (1968).

11. Lindholm U. S., Yeakley L. M. and Nagy A. The dynamic strength and fracture properties of Dresser Basalt. Int. J. Rock Mech. Min. Sci. & Geomech. Abst. 11, 181 (1974).

12. Logan J. M. and Handin J. Triaxial compression testing at intermediate strain rates. Dynamic Rock Mechanics - Proc. Twelfth Symp. on Rock Mechanics (Ed. G. B. Clark), p. 167, AIME, New York (1971).

13. Mellor M. and Hawkes I. Measurement of tensile strength by diametrical compression of discs and annuli. Eng. Geol. 5, 173 (1971).

14. Perkins R. D., Green S. J. and Friedman M. Uniaxial stress behavior of porphyritic tonalite at strain rates to 10^3/second. Int. J. Rock Mech. Min. Sci. 7, 527 (1970).

15. Price D. G. and Knill J. L. A study of the tensile strength of isotropic rocks. Proc. 1st Congr. Intern. Soc. Rock Mech., Lisbon, 439 (1966).

16. Price N. J. Rates of deformation. J. Geol. Soc. 131, 553 (1975).

17. Roberts D. K. and Wells A. A. The velocity of brittle fracture. Engineering 178, 820 (1954).

18. Schock R. N. and Heard H. C. Static mechanical properties and shock loading response of granite. J. Geophys. Res. 79, 1662 (1974).

19. Shockey D. A., Petersen C. F., Curran D. R. and Rosenburg J. T. Failure of rock under high rate tensile loads. New Horizons in Rock Mechanics - Proc. Fourteenth Symp. on Rock Mechanics (Ed. H. R. Hardy Jr.), p. 709, AIME, New York (1973).

20. Stowe R. L. and Ainsworth D. L. Effect of rate of loading on strength and Young's modulus of elasticity of rock. Basic and Applied Rock Mechanics - Proc. Tenth Symp. on Rock Mechanics (Ed. K. E. Gray), p. 3, AIME, New York (1972).

21. Whitten C. A. Crustal movements in California and Nevada. Am. Geophys. Un. Trans. 37, 393 (1956).

APPENDIX A: DATA REDUCTION

The following formulae are used to obtain the numbers in Tables 3-5 (pp. 19-23) from the experimental records (Fig. 22).

1. Apparent differential stress at failure.

$$\sigma_a = (F_1 - F_o)/A$$

2. Strain at failure.

a. Charcoal Granodiorite.

$$e = u_s/L$$

where the displacement between the ends of the specimen is given by

$$u_s = u_1 - u_o - (F_1 - F_o - m \frac{d^2u}{dt^2})/k_m \qquad (14)$$

No correction is made for the effect of the epoxy fillets because the modulus of the epoxy is about 2 GPa as compared to about 50 GPa for that of the Charcoal Granodiorite.

b. Berea Sandstone and Indiana Limestone. A correction is made for the dogbone configuration based on the following analysis. The strains in each segment of the specimen, as shown in Fig. 23, are given by

$$e_1 = \frac{\Delta L_1}{L_1} = \frac{F}{EA_1}$$
$$e_2 = \frac{\Delta L_2}{L_2} = \frac{F}{EA_2} \qquad (15)$$
$$e_3 = \frac{\Delta L_3}{L_3} = \frac{F}{EA_3}$$

where $$\Delta L_1 + \Delta L_2 + \Delta L_3 = u_s \qquad (16)$$

$F \equiv$ axial force

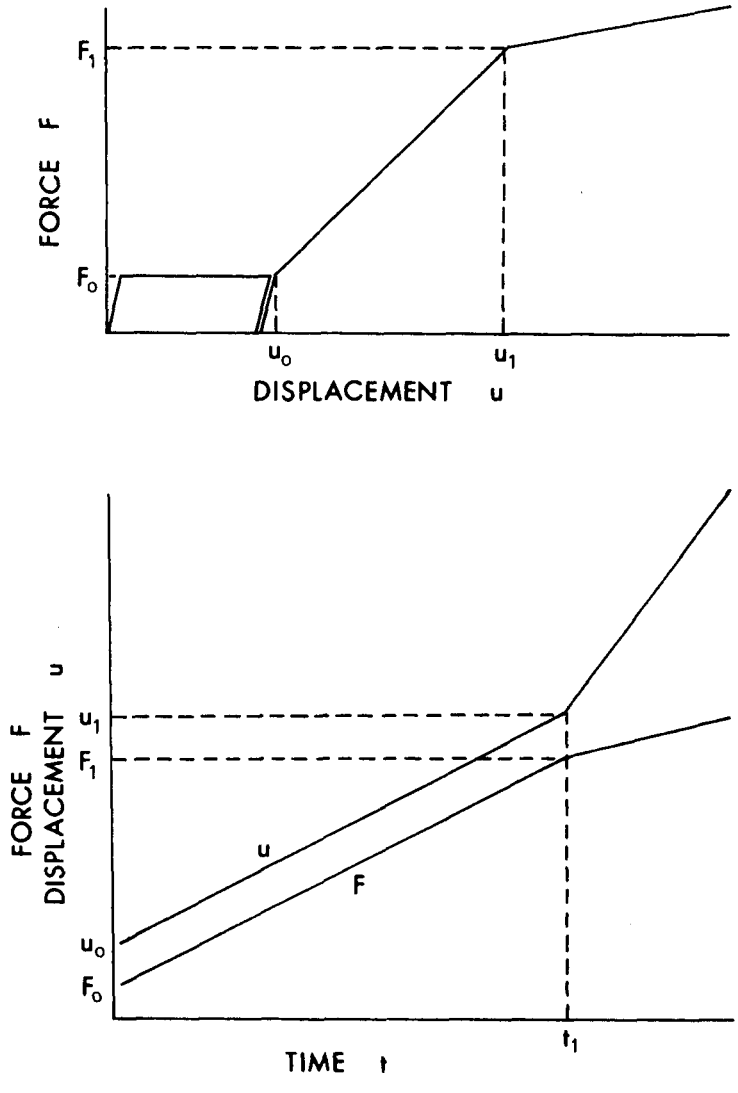

Figure 22. Idealized experimental records. F_0, frictional force between piston and packing gland; F_1, force at failure; u_0, displacement necessary to seat specimen; u_1, displacement at failure; t_1, time at failure.

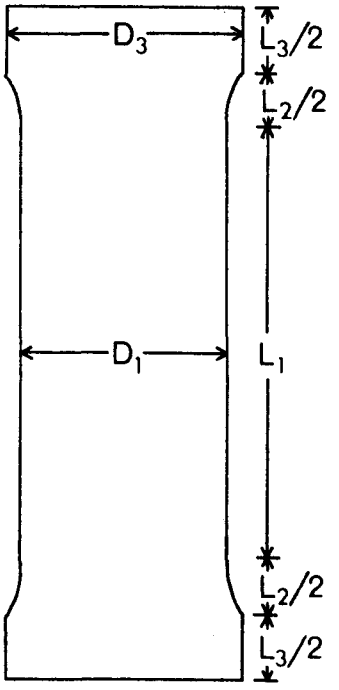

Figure 23. Dimensions used in correcting for effect of dogbone configuration on strain. D_1, gage diameter; D_3, head diameter; L_1, gage length; L_2, tapered length; L_3, head length.

$$E \equiv \text{modulus}$$

$$A_1 \equiv \pi\left(\frac{D_1}{2}\right)^2$$

$$A_2 \equiv \pi\left(\frac{D_1 + D_3}{4}\right)^2$$

$$A_3 \equiv \pi\left(\frac{D_3}{2}\right)^2$$

The four equations, 15 and 16, have four unknowns, F/E, ΔL_1, ΔL_2, and ΔL_3, so that the system is exactly determined, and the following solution can be obtained for the strain in the portion of the specimen with the reduced diameter:

$$e_1 = \frac{\Delta L_1}{L_1} = \frac{u_s}{L_1\left[1 + \frac{A_1}{L_1}\left(\frac{L_2}{A_2} + \frac{L_3}{A_3}\right)\right]}$$

3. Log everage strain rate.

$$\log \dot{e} = \text{Log } (e/t_1)$$

4. Error propagation. Let $x_i \pm \Delta x_i$ be the individual measurements used to calculate the results, $y_j \pm \Delta y_j$, in Tables 3-5 (pp. 19-23). The errors, Δy_j, are calculated by the following formulae

a. Sum and difference.

$$y_j = x_1 \pm \ldots \pm x_n$$

$$\Delta y_j = \left(\Delta x_1^2 + \ldots \Delta x_n^2\right)^{1/2}$$

b. Product and quotient.

$$y_j = \frac{x_1 \ldots x_k}{x_{k+1} \ldots x_n}$$

$$\Delta y_j = \left[\left(\frac{\Delta x_1}{x_1}\right)^2 + \ldots + \left(\frac{\Delta x_n}{x_n}\right)^2\right]^{1/2} / y_j$$

c. Log function.

$$y_j - \log x_i$$

$$\Delta y_j = \Delta \log x_i = \Delta x_i \frac{d}{dx_i} \log x_i = \Delta x_i \frac{d}{dx_i} \left(\frac{\ln x_i}{\ln 10}\right)$$

$$= \frac{\Delta x_i}{x_i \ln 10}$$

APPENDIX B: DERIVATION OF EQUATIONS USED IN MODEL

1. Solution of equation of motion. With the force function used in the model, equation 1 becomes

$$rt = (m \frac{d^2}{dt^2} + c \frac{d}{dt} + k)\, u(t) \tag{17}$$

With initial conditions

$$u(o) = \frac{du}{dt}\Big|_{t = o} = \frac{d^2u}{dt^2}\Big|_{t = o} = 0$$

the Laplace transform method can be used to solve equation 17. The following notation is used for the Laplace transform,

$$\overline{f}(s) = \int_o^t f(t) \exp(-st)dt$$

The Laplace transform of equation 16 is

$$r/s^2 = (ms^2 + cs + k)\, \overline{u}\,(s)$$

$$\overline{u}\,(s) = \frac{r}{s^2(ms^2 + cs + k)} \tag{18}$$

The inverse Laplace transform of equation 18 is found by

$$u(t) = \frac{1}{2\pi i} \int_{c - i\infty}^{c + i\infty} \overline{u}\,(s) \exp(st)\, ds$$

This yields the following solution to equation 16,

$$u(t) = \frac{r}{k}\{t - \frac{c}{k}[1 - \exp(-at)(\cos bt + \frac{a^2-b^2}{2ab}\sin bt)]\} \qquad (2)$$

2. Failure criteria.

a. Constitutive relation under model conditions.

Let $\sigma(t) \equiv f(t)/A$ (19)

where $f(t) \equiv F(t) - m\frac{d^2u}{dt^2}$

$= (k + c\frac{d}{dt})\,u(t)$ (20)

From equation 2, we have

$$\frac{du}{dt} = \frac{r}{k}\,q \qquad (21)$$

and $$r = \frac{k}{p}\,u(t) \qquad (22)$$

Combining equations 21 and 22 gives

$$\frac{du}{dt} = \frac{q}{p}\,u(t)$$

Thus equation 20 becomes

$$f(t) = (k + c\frac{q}{p})\,u(t) \qquad (23)$$

The displacement associated with the specimen is

$$u_s(t) = (1 - \frac{k}{k_m})\,u(t) \qquad (24)$$

Combining equations 23 and 24 gives

$$f(t) = k_s \left(1 + \frac{c}{k} \frac{q}{p}\right) u_s (t) \tag{25}$$

Let the strain be

$$e(t) \equiv u_s(t)/L \tag{26}$$

From equations 19, 25, and 26, we have the following stress-strain relation

$$\sigma(t) = \frac{L}{A} k_s \left(1 + \frac{c}{k} \frac{q}{p}\right) e(t) \tag{27}$$

b. Stress criterion. The condition given by equation 7 is

$$\sigma(t_1) \equiv \sigma_1 \tag{7}$$

Combining this with equation 27 gives equation 8,

$$e(t) = \frac{A \sigma_1}{L k_s \left(1 + \frac{c}{k} \frac{q}{p}\right)} \tag{8}$$

In practice, equation 14 is used instead of equation 24, as follows,

$$u_s(t) = u(t) - \left(F(t) - m \frac{d^2u}{dt^2}\right) / k_m$$

$$= u(t) - f(t)/k_m \quad \text{by equation 20.}$$

Combining this with equation 23 gives

$$u_s(t) = \left(\frac{1}{k + c\frac{q}{p}} - \frac{1}{k_m}\right) f(t) \tag{28}$$

Equation 9 can now be derived from equations 7, 19, 26, and 28:

$$e(t) = \frac{A}{L}\sigma_1 \left(\frac{1}{k + c\frac{q}{p}} - \frac{1}{k_m}\right) \tag{9}$$

A graphical comparison of equations 8 and 9 is shown in Fig. 24.

c. Strain criterion. The condition given by equation 11 is

$$e(t_1) \bar{=} e_1 \tag{11}$$

Combining this with equation 27 gives equation 12,

$$\sigma\ (t_1) = \frac{L}{A} k_s \left(1 + \frac{cq}{kp}\right) e_1 \tag{12}$$

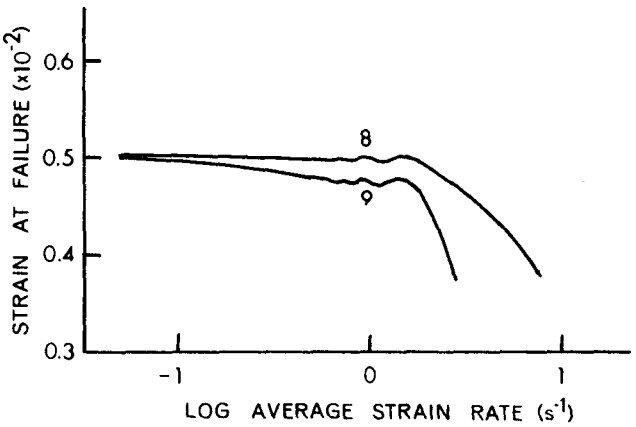

Figure 24. Comparison of curves for strain at failure given by equations 8 and 9.

APPENDIX C: WAVE AND CRACK PROPAGATION VELOCITIES

The following equations are used in calculating the values given in Table 6.

1. Wave velocity:

$$v_w = (E/\rho)^{1/2}$$

where $E \equiv$ dynamic Young's modulus

ρ = density

See Table 2 (p. 13) for values of E and ρ.

2. Number of times a wave can travel the radius, R, of the specimen in the time, t_1, of the fastest tests ($\simeq$ 3 ms):

$$n_w = t_1 \, v_w / R$$

3. Crack propagation velocity [17]:

$$v_c = 0.38 \, (E/\rho)^{1/2}$$

4. Number of times a crack can propagate the length, L_1, of the specimen in the time of the fastest tests:

$$n_c = t_1 \, v_c \, / \, L$$

Table 6. Wave and crack propagation velocities.

Rock	v_w (km/s)	n_w	v_c (km/s)	n_c
Charcoal Granodiorite	4.22	1990	1.60	96
Berea Sandstone	2.01	730	0.76	46
Indiana Limestone	4.02	1460	1.53	92